Physica D 454 (2023) 133866

Contents lists available at ScienceDirect

Physica D

journal homepage: www.elsevier.com/locate/physd

The power of weak, transient interactions across biology: A paradigm of emergent behavior☆

Paula A. Vasquez [a], Ben Walker [b], Kerry Bloom [c], Daniel Kolbin [c], Neall Caughman [d], Ronit Freeman [e], Martin Lysy [f], Caitlin Hult [g], Katherine A. Newhall [d], Micah Papanikolas [e], Christopher Edelmaier [e,h], M. Gregory Forest [d,e,*]

[a] Department of Mathematics, University of South Carolina, United States of America
[b] Department of Mathematics, University of California at Irvine, United States of America
[c] Department of Biology, University of North Carolina at Chapel Hill, United States of America
[d] Department of Mathematics, University of North Carolina at Chapel Hill, United States of America
[e] Department of Applied Physical Sciences, University of North Carolina at Chapel Hill, United States of America
[f] Department of Statistics and Actuarial Science, University of Waterloo, Canada
[g] Department of Mathematics, Gettysburg College, United States of America
[h] Center for Computational Biology, Flatiron Institute, United States of America

ARTICLE INFO

Article history:
Received 5 March 2023
Received in revised form 19 July 2023
Accepted 25 July 2023
Available online 4 August 2023

Keywords:
Biological paradigm
Weak
Transient interactions
Emergent behavior

ABSTRACT

A growing list of diverse biological systems and their equally diverse functionalities provides realizations of a paradigm of emergent behavior. In each of these biological systems, pervasive ensembles of weak, short-lived, spatially local interactions act autonomously to convey functionalities at larger spatial and temporal scales. In this article, a range of diverse systems and functionalities are presented in a cursory manner with literature citations for further details. Then two systems and their properties are discussed in more detail: yeast chromosome biology and human respiratory mucus.

1. Introduction

We present multiple examples across biology where a complex functionality is a consequence of simplicity — mixtures of molecular species and their physical and chemical interactions. While Earth is sufficiently rich to provide the ingredients that make life possible, those ingredients have to work together without oversight and intervention to endow a complex function. In eukaryotic organisms, cells manufacture large molecular weight polymers (e.g., chromosomal DNA, mucins) plus additional molecular species that, without each other, do not convey functionality (e.g., transcription, a protective barrier). They become powerful and functional by pervasive and transient *local* interactions acting on and between the polymers. The local sources are *either* basic monomeric units of polymer chains (e.g., glycosylated brush-like domains within mucins [13,14] that exhibit transient hydrophobic self-interactions) *or* third-party proteins that chemically activate local domains within large molecules (e.g., structural maintenance of chromosome proteins that transiently crosslink genes within and between chromosomes [15]). We survey these two biological systems below. In other instances, cells utilize basic principles of molecular complex formation through transient binding–unbinding interactions and

☆ This article is dedicated to the memory of Hermann Flaschka, mathematician extraordinaire. I collaborated with Hermann and Dave McLaughlin (my primary adviser) as a graduate student at the University of Arizona, leading to the paper [1]. Dave and Hermann were always tuned in to emerging paradigms, of course the many mathematical facets of integrable systems, as well as the developments in chaotic dynamical systems. Theoretically and computationally with Dave and Nick Ercolani [2], and with Dave, Alan Bishop, Randy Flesch, and Ed Overman [3,4], together with subsequent contributions by Li and McLaughlin [5], Ablowitz and Herbst [6], Kovačič and Wiggins [7], Oliver and Stern [8], and many others, we collectively realized and amplified that these two paradigms were intertwined through physical perturbations as well as numerical discretizations of modulationally unstable wavetrain solutions of the sine–Gordon equation (the wave equation generalization of the pendulum) and the focusing nonlinear Schrodinger equation (arising in diverse applications including nonlinear optics). Hermann's international reputation, emanating from his ingenious integration of the Toda lattice [9–12], was palpable in every trip abroad to soliton meetings starting in 1980. It never failed that I was asked "what is Hermann working on?" in the futile hope that I would know and confide.

* Corresponding author at: Department of Mathematics, University of North Carolina at Chapel Hill, United States of America.
E-mail address: forest@unc.edu (M.G. Forest).

https://doi.org/10.1016/j.physd.2023.133866
0167-2789/

then allow entropic phase separation to sequester the larger complexes without the need for costly membranes. Specific molecular complexes or self-organized structures are essential within living organisms to carry out diverse functions. Some examples at the cellular scale are nuclear organization, transcription of messenger RNA sequences, protein manufacture, and efficient searches of damaged DNA for homologous chromosomes for DNA repair. At the tissue and organ scale examples include protective mucus barriers on organs, e.g., to immobilize pathogens or toxic species and facilitate removal in the respiratory and reproductive tracts, or to create a pH barrier in the stomach. Additional instances underlie alternative means of protection, e.g., release of cytokines post infection that signal immune agents to the site of infection. More details can be found in the papers referenced for the various biological systems listed below.

Across biology, scale-separated biomolecular players (large polymers or complexes and small proteins) undergo weak, transient interactions. These physicochemical ingredients autonomously instill a dazzling array of functionalities: dynamic gene organization to carry out necessary cellular functions throughout the cell cycle; network structure with rapid response–recovery properties to accomplish mucus trapping of inhaled insults and clearance by coordinated cilia; neutralization or immobilization of viruses and bacteria in organ mucus barriers; formation and sequestering of molecular complex compartments without the need for membranes; and other functionalities as given in the list of examples below. In each of these systems, applied mathematicians have teamed with domain experts from chromosome and cellular biology, biochemistry, biophysics, pulmonary medicine, and pharmacy, working synergistically in the quest to understand these highly complex systems from first principles. We tell this story through the lens of the *collective* collaborations and results of the authors so that the commonality of the paradigm of the strength of weak binding becomes evident.

It is fair to state that today, domain experts argue that their biological system is too complicated, and the experimental data too difficult to interpret, without mechanistic modeling based on chemistry, mathematics, and physics principles. Such model foundations allow formulation and testing of hypotheses. They also allow the ability to use images, static or dynamic, from various instruments as truth sets from which numerical sweeps and optimization methods can be performed at different levels. Such virtual experiments are obviously impossible to perform in the lab. Through the feedback between *in silico* and *in vivo* data and the exploration of sufficient mechanisms to understand the phenomena of interest, we learn hidden principal mechanistic components, and estimate weak interaction strengths with confidence intervals bounded by experimental data. It is a luxury of collaborative science to have domain experts willing to do the work necessary to build this experimental-modeling partnership. Our predictive, computational, mathematical platforms are modern, biological analogs of the rich history of applied mathematics in fluid mechanics, aerodynamics, and diverse engineering applications. Our modeling platforms incorporate the physics and chemistry specific to the biomolecular players and their multiscale spatio-temporal interactions. Together with experimental design and data, *our collective aim is to learn how the unobservable ensemble of pervasive, local, weak interactions leads, autonomously, to the observable coarse-grained, emergent behavior and functionality*. The modeling platform affords flexibility and freedom to explore, and sometimes learn, system features associated with both optimal and robust functionality, as well as pathways to recovery from system features associated with dysfunction.

Below is a list of biological systems and functionalities, plus collaborators, that reflect the paradigm of emergent behavior from many weak interactions. We refer the reader to our published work for background motivation, experimental and theoretical progress and open questions, and comprehensive literature citations, for the systems 3–8 listed below, and provide a brief summary of these aspects of systems 1 and 2 in Sections 2, 3, 4.

1. Spatial and dynamic self-organization of the genome in the nuclei of living cells (MG. Forest, K. Bloom lab, J. Lawrimore, P.A. Vasquez, D. Adalsteinsson, C. Hult, B. Walker, D. Taylor, Y. He, K. Newhall, A. Ford, X. Cao, C. Edelmaier, and others).
   This system is discussed further in Section 2.
2. Structure, macrorheology, passive and active microrheology to characterize and discern healthy versus disease-modified respiratory mucus (MG Forest, R. Superfine, D. Hill, R. Boucher, J. Sheehan, C.W. Davis, M. Rubinstein, S. Mitran, R. Camassa, R. McLaughlin, C. Hohenegger, S. McKinley, P.A. Vasquez, M. Lysy, N. Pillai, R. Freeman, M. Markovetz, M. Papanikolas, X. Cao, C. Edelmaier, A. Ford, N. Caughman, and others).
   A pan-university initiative at UNC-Chapel Hill brought together researchers from Applied Mathematics, Physics, Chemistry, and the Cystic Fibrosis Center to form the Virtual Lung Project. One of the main contributions from the applied math side was to adapt the rheological instruments and computational polymer hydrodynamics toolbox to characterize mucus from the human respiratory tract across health and disease. Cystic fibrosis was the primary disease target, together with asthma and COPD. Twenty-five years later, we continue to gain new insights into the dramatic distinctions between engineered polymeric materials and Nature's polymers — namely, the paradigm of weak, transient interactions within and between the mucin polymers that comprise respiratory mucus as well as the mucus barriers throughout the human body. Various aspects of human respiratory mucus, mathematical models of mucus and its rheological properties (how it responds at different levels of stress or strain), and the role of mucin-polymer transient interactions in disease progression of cystic fibrosis are described in Sections 3, 4.
3. Immobilization of pathogens (passive and active) in the mucus barriers of the cervicovaginal and intestinal tract [16–23]; physiology-based viral infection in the human respiratory tract and COVID-19 (MG Forest, S. Lai lab, R. Freeman lab, R. Boucher, R. Pickles, A. Chen, T. Wessler, J. Newby, S. McKinley, M. Jensen, J. Pearson, A. Aristotelous, and others) [24–27].
   From sexually transmitted diseases, including HIV, to stomach infections, seasonal colds, and flu, and now COVID-19, the explicit and often leading-order protective roles of the mucus barrier in the cervicovaginal tract, gut, and respiratory tract were not previously embedded in mathematical models of within-host infection. Our work has focused on understanding the critical roles of organ mucus barriers, and in translation of experimental-modeling insights into medical and public health solutions.
4. Reversible transitions between bleb-like and stretched morphologies of the cell membrane–cortex couple, (MG Forest, K. Jacobson lab, M. Kapustina, D. Tsygankov, J. Zhao, T. Wessler, A. Chen, T. Elston, Q. Wang) [28,29].
   Led by our dear colleague Ken Jacobson who recently passed away, we were introduced to several remarkable features of cells that are essential for adaptation to different stimuli and interfacial conditions, and thereby for survival. Ken and lab partner Maryna Kapustina focused on aspects of the cell surface membrane and adjoining cortical layer. Transitions between a stretched and smooth surface morphology while

anchored to a substrate and a rounded morphology with a skewed distribution of bleb-like protrusions occurs too fast for membrane remodeling, therefore cells are equipped with a significant excess of surface membrane. What functions do excess surface area allow? How is the membrane–cortex couple chemically activated for motility and for switching between a smooth morphology on a substrate versus the highly irregular, bleb-like morphology that oscillates after being released from the substrate? Our group developed a diversity of mechanistic computational models to understand the interplay and coupling between chemical signaling, surface physics and mechanics of the membrane and cortex, and to replicate experimental behavior and properties.

5. Sequestration of cytoplasmic condensates in cells by liquid–liquid phase separation (MG Forest, A. Gladfelter lab, J. Newby, K. Gasior, J. Zhao, Q. Wang) [30–32].
   Amy Gladfelter's lab explores the physical and chemical processes by which cells create molecular complexes sustained by transient binding–unbinding kinetics of sub-species of the complex and sequester the complexes into compartments in order to perform essential cellular processes. To avoid the cost and limitations of membranes to sequester complexes, cells routinely exploit liquid–liquid phase separation. Once again, our modeling group borrowed and extended classical Cahn–Hilliard type phase field models tailored to the molecular species and complexes within the cytoplasm of multi-nuclear fungi, and to understand how these organisms use spatial heterogeneity to prevent synchrony of nuclei.
6. Molecular motor transport of cargo along microtubules (MG Forest, J. Newby, K. Patel, S. Mao, S. Lai) [33].
   The applied mathematics community has invested significantly to understand the behavior of molecular motors that transiently bind, unbind, and travel along microtubules. Similar to how antibodies co-bind to spikes on viruses and domains on mucin polymers, dynein and kinesin motors also co-bind, either to transport cargo along microtubules, or to bridge neighboring microtubules and drive cilia and flagella beat cycles. This project was from undergrad research by Patel and Mao, using stochastic modeling to show that weak binding of kinesin to microtubules enhances cargo transport.
7. Drug delivery (MG Forest, Lai lab, Y. Cao, A. Talkington, T. Wessler) [34–39].
   Modeling of drug delivery either to tumors or specific organs via the circulatory system has risen dramatically to assist in clinical trials or animal trials for a variety of benefits: establish efficacy, improve site-specific targeting, and identify unintended consequences, all leading to faster approval of efficacious drugs. Our group has developed physiologically based, pharmacokinetic (PBPK) models to accompany animal experiments and clinical trial data to address open questions from our colleagues in pharmacy (Cao and Lai). One such question has arisen from the use of polyethylene glycol (PEG) as a drug delivery solvent to prolong circulation of the drug, and the strong empirical and subsequent mouse model evidence that individuals previously exposed to PEG from personal products has led to anti-PEG antibodies that act to remove the PEGylated drug carriers from the circulatory system. This led to a cocktail strategy to minimize this effect by introducing a PEG dose to dilute the anti-PEG antibodies and then follow with the PEGylated drug dosage.
8. Synthetic materials science (Sloan Foundation collaborative group, MG Forest, R. Freeman, A. Gladfelter, K. Hahn, R. Baker, E. Nazockdast, C. Edelmaier, D. Klotsa) (publications forthcoming).
   The purpose of this Sloan Foundation funding is to first learn how Nature and biology use biomolecular mixtures to perform functions at the molecular to tissue to organ to organism scale, and then to engineer materials with life-like properties. A key element of this effort is understanding how different aspects of the weak binding paradigm can be leveraged.

2. Spatial and dynamic self-organization of the genome in the nuclei of living cells

The Bloom lab at UNC-CH uses budding yeast *(Saccharomyces cerevisiae)* as a model system to study the genome of a living organism. The yeast genome has about 14 million base pairs (fundamental molecular unit) packaged into 16 pairs of chromosomes with around 6 thousand genes (fundamental functional unit) and was the first eukaryotic genome to be sequenced in 1996 [40]. In comparison to the yeast genome, the human genome has about 6 billion base pairs packaged into 23 pairs of chromosomes with around 30 thousand protein-coding genes and a hundred-times more non-coding genes. Remarkably, a complete human genome was only recently published in 2022 [41]. The yeast genome is simpler, obviously available, free of ethical concerns, and as such it is widely used to study gene regulation, DNA replication, and disease. Most importantly it shares many cellular processes with the human genome such as cell division and DNA replication and repair, among others. Consequently, understanding of a simpler system such as the yeast cell has led to impactful insights into human diseases [42–46].

The Bloom lab specializes in experiments with single living cells in contrast with the more prevalent approaches using chromatin conformation capture (3C). High-throughput 3C experiments have been carried out on many eukaryotic organisms, from yeast to humans [47,48]. In this approach, cells are exposed to formaldehyde which render them 'frozen' at a given time in the cell life cycle, then gene-specific tagging reveals gene location across all chromosomes, giving a matrix of gene–gene interaction of all genes on all chromosomes and providing important insight into gene–gene dynamics. In this way, population averages over thousands of dead cells yield inferences about global two-point statistics of genome organization. In Sections 2.2.5–2.2.7 we introduce higher-order statistics of gene organization that optimizes both, based on spatial proximity and persistence in time [49]; see Fig. 8. In contrast, single-cell experiments use live imaging data from fluorescently tagged domains on specific base pair sequences, genes, and chromosomes for individual living cells. The data gathered from these experiments allow for a more direct connection with dynamic simulations and a better understanding of the intricacies involved in different cellular functions. The advantage of creating models based on single cell experiments is that it is always possible to scale up results to be compared with 3C experiments, while averaged data cannot always be used to describe individual cells nor their dynamics. Indeed, we have shown that time-averaging of spatially resolved single-cell data obscures structural gene organization into dynamic communities of genes, see Fig. 7 [50].

Nonetheless, both single cell and Hi-C (extensions of 3C) experimental approaches have shown that chromosomes are not distributed randomly in the nucleus. The organization of the genome in the nucleus can be studied at different length scales shown in Fig. 1 *[51,52]*. (i) At the lower scale, between 1 base pair (bp) and several thousand base pairs (kb), the genome adopts a beads-on-a-string structure, ∼11 nm in diameter, formed by nucleosomes and DNA. Above the 11-nm fiber, the structure is irregular and dynamically samples many conformations and the details of folding are still uncertain [51]. (b) At length scales on the order of the nuclear domain (micron scale $>$ 100 Mb or mega base pairs), the genome is divided into chromosomes, each of which occupies statistically defined territories [53–56].

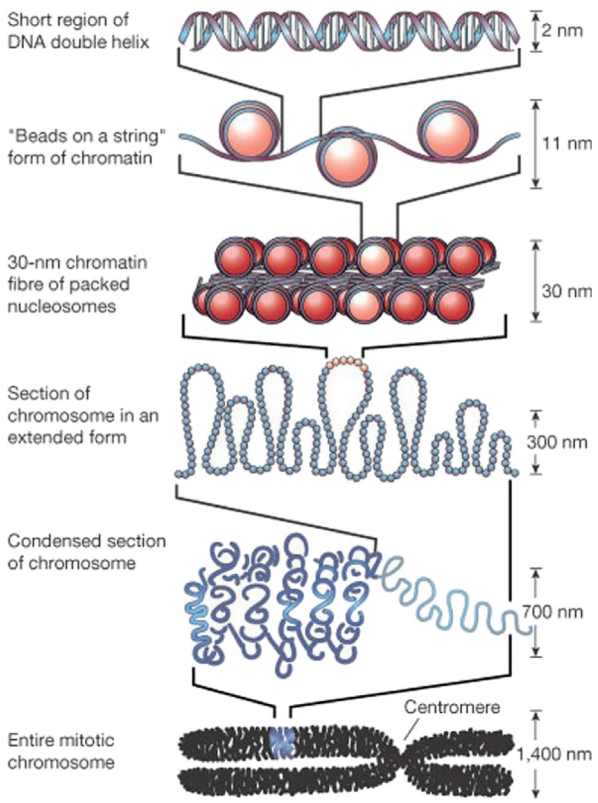

Fig. 1. Levels of DNA packing into chromosomes.
Source: Figure adapted from [51].

(c) At intermediate and large length scales (∼Mb), organization differs from cell to cell, but it is known that the genome is not randomly organized and that its spatial organization plays a key role in the execution of a variety of nuclear functions [57–59]. For a review of different physical and organizational structures inside the nucleus at this level the reader is referred to [60]. It follows, that understanding the spatial dynamics of the genome within the nucleus is a crucial step in characterizing how DNA adopts and transitions between different functional states over the course of the cell cycle, facilitating a wide range of vital functions. While a great part of our understanding of the physical properties of chromatin organization and its role in cell functions has come from experimental observations, it has become clear that a more complete understanding of chromatin as a physical structure requires an integration between biology and mathematical modeling, in particular models derived from polymer physics. For instance, there is an ongoing conversation to determine to which extent the chromosomes are passive fibers whose organization is fully dictated by active enzymatic-driven processes or if chromosomes are active entities whose intrinsic physical properties play a primary role in the genome organization. As is often the case in biological systems, it is likely that both passive and active chromosome-based mechanisms will be found, depending on the particular process. Single cell experiments in live cells together with the polymer models discussed below are fitted to better answer these questions.

Close integration of experimental data and computational modeling had already led to significant insights into some basic principles of the 3D architecture of chromosomes during interphase and mitosis [54,62–65]. An exhaustive review of these approaches is out of the scope of the present review. Instead, here we focus on a specific part of the cell cycle – interphase – and a particular class of models — bead–spring polymeric models. These models are of particular interest since it has been shown that the spatial architecture and dynamics of yeast chromosomes can be well understood from the random motions of semiflexible polymer chains tethered at the centromeres and telomeres [53,56,66–68]. In short, understanding the mechanisms controlling chromosome behavior *requires integration* (as advocated in the 4D Nucleome Project [69] and updated at the time of this writing in [70]) of cell biology, diverse experimental probes (microscopy of live cells [54,71–75]) together with Hi-C techniques applied to massive numbers of stationary cells [47,76–78], coupled with physical principles that govern fluctuating polymer chains and the small structural proteins that transiently act on them to steer dynamic organization.

2.1. Stochastic polymer "bead–spring" models of chromatin

In this approach a chromosome arm is modeled as a polymer chain constrained within a nuclear envelope and tethered to the boundary, as shown in Fig. 2. Following polymer physics, each chain is represented by a series of N beads connected via nonlinear springs and the equation of motion for the ith bead is obtained from a force balance in the zero-mass limit,

$$\boldsymbol{F}_i^D + \boldsymbol{F}_i^S + \boldsymbol{F}_i^{EV} + \boldsymbol{F}_i^W + \boldsymbol{F}_i^B = \boldsymbol{0}. \tag{1}$$

- **Drag force, $\boldsymbol{F}_i^D$**
  As a first approximation, the drag force is assumed to be linear, $\boldsymbol{F}_i^D = -\zeta \frac{d\boldsymbol{X}_i}{dt}$, where ζ is the drag coefficient of a bead and $\boldsymbol{X}_i$ its position. For simplicity, anisotropic drag, and other types of hydrodynamic interactions (HIs) are not included. In particular, HIs in bead–spring models have been shown to be negligible for weak and "crowded" flows [79,80], as is the case in the nucleus. The relative influence of HIs is an open question, with experimental and computational evidence of large-scale induced flow [81–83] not captured without HIs.
- **Spring force, $\boldsymbol{F}_i^S$**
  This force derives from a restoring potential from bead–bead displacements. In the nucleus, forces affecting DNA interactions are many with some not completely understood. Because of this lack of complete knowledge of all potentials affecting strains of chromosome chains, instead of modeling several sources of restoring forces, all forces are clumped into a single form. In this work we use a worm-like-chain model proposed by Marko and Siggia [84,85], that describes the non-linear variation in $\boldsymbol{F}$ as a function of DNA extension, and which has been shown to accurately describe the dynamics of chromatin in vivo [86]:

$$\boldsymbol{F}_i^S = \boldsymbol{F}_{i,j-1} + \boldsymbol{F}_{i,j+1}, \tag{2}$$

$$\boldsymbol{F}_{i,j} = \frac{k_B T}{4L_p}\left[\left(1 - \frac{R_{ij}}{R_0}\right)^{-2} - 1 + 4\frac{R_{ij}}{R_0}\right]\frac{\boldsymbol{R}_{ij}}{R_{ij}},$$

$$\boldsymbol{R}_{ij} = \boldsymbol{X}_i - \boldsymbol{X}_j, \quad R_{ij} = \sqrt{\boldsymbol{R}_{ij}\cdot\boldsymbol{R}_{ij}}, \quad R_0 = N_{k,s}\left(2L_p\right).$$

  Here L_p is the persistence length of the chromatin fiber and $N_{k,s}$ is the number of Kuhn lengths per spring, which translates to the level of discretization used to define the number of beads that describe a chromosome chain. k_BT is the Boltzmann constant times absolute temperature. At physiological temperatures for cellular growth, $k_BT = 4.1$ pN nm. The force equation above describes the non-linear variation in $\boldsymbol{F}$ as a function of DNA extension. The parameter R_0 controls the maximum extensibility of the spring: as R_{ij} approaches R_0 the force rapidly increases preventing the length of the spring from exceeding that value. Physically, R_0 is equivalent to the contour length of the chain. This equation accurately describes the linear elastic response at low extension

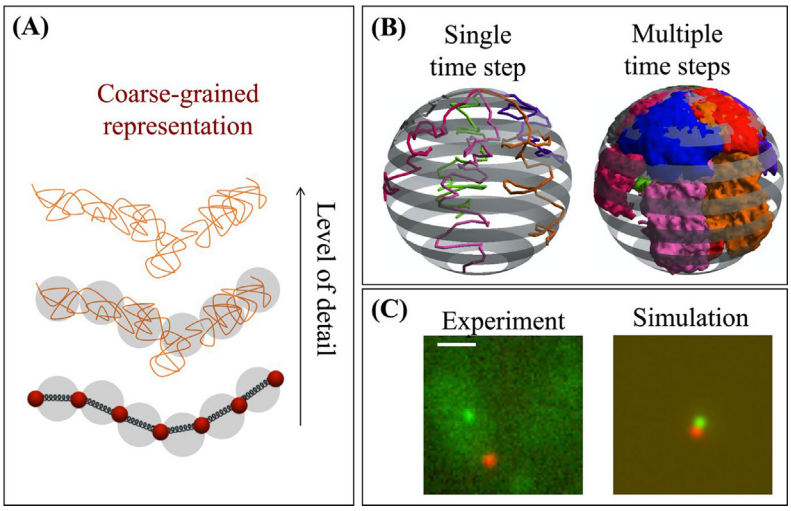

Fig. 2. (A) Coarse grained representation of chromosomes. *Top*, depiction of a DNA chain (greatest detail). *Middle*, DNA coarse grained depiction of thermal (tension) blobs in gray. *Bottom*, graphical depiction of the mathematical model where each blob is represented by red beads connected via springs. (B) Simulation of chromosomes as polymer chains tethered to the nuclear envelope results in the formation of territories. *Left*: A single time step from the bead–spring model. Chromosomes are depicted as chains (colored lines) confined to the nucleus (nuclear sphere indicated by parallel gray bands). *Right*: Space filling view of chromosomes when multiple time steps are visualized to portray chromosome territories (colored masses) representing the extent of motion of individual chromosomes. (C) Simulated data can be directly compared with experimental data of individual, live cells. *Left*: Cells containing fluorescent labels on a single chromosome. Green: gene repressor protein (LacI) fused to green fluorescent protein GFP, bound to its binding site (Lac operator) integrated into a specific location in a yeast chromosome. Red: site within the nuclear envelop where the chains are tethered, north pole in panel (B), known as the spindle pole body. A protein component of spindle pole body is fused to a red fluorescent protein. *Right*: Simulated image in which we have computationally added fluorphores (sources of light) to one of the beads of the chain (green) or the north pole in the model (red). The light sources are computationally diffused to match the spread of light as it passes through the point spread function (PSF) of the microscope objective [61]. In this way we can directly compare simulated images and dynamics to experimental material. Scale Bar = 1 μm.

regimes $\left(R_{ij} \ll R_0\right)$ as it reduces to Hooke's law. As R_{ij} approaches R_0, $\left(R_{ij} \sim R_0\right)$, the force rapidly increases due to the increasing entropic cost of extending covalent bonds within the DNA molecule.

– **Excluded volume force, $\boldsymbol{F_i^{EV}}$**
This force imposes an energy penalty on the overlapping of two beads. Just as was the case with the spring forces, the model coarse grains all repulsive forces into a single potential. We use the excluded volume potential introduced by Jendrejack et al. [87],

$$\boldsymbol{F}_i^{EV} = -\nabla U_i^{EV}, \tag{3}$$

$$U_i^{EV} = \frac{\nu k_B T}{2}\left(\frac{3}{2\pi S_k^2}\right)^{3/2} \sum_{\substack{i,j=1 \\ i \neq j}}^{N} \exp\left[-\frac{3\boldsymbol{R}_{ij}^2}{2S_k^2}\right], \qquad S_k^2 = N_{k,s}\frac{\left(2L_p\right)^2}{6}.$$

If we consider the limit where this Gaussian potential goes to a δ-function, it can be shown that the overlapping between two beads has an energy penalty of ν k_BT, where ν is the excluded volume parameter, with k_BT defined above.

– **Interaction with the nuclear wall, $\boldsymbol{F_i^W}$**
This force mimics confinement within the nucleus. However, in our simulations we do not include an explicit form for the force, instead the position of a bead that has moved between timesteps from inside to outside the nuclear wall is reflected back inside by

$$\boldsymbol{X}_i^{\text{new}} = \boldsymbol{X}_i^{\text{out}} + \Delta\boldsymbol{X}_i^{\text{HM}}, \tag{4}$$
$$\Delta\boldsymbol{X}_i^{\text{HM}} = \Delta p_i H\left(\Delta p_i\right).$$

Here $\Delta\boldsymbol{X}_i^{\text{HM}}$ is the displacement vector due to the Heyes–Melrose algorithm [88], Δp_i is the difference from the position of the bead outside the domain boundary, $\boldsymbol{X}_i^{\text{out}}$, to the nearest boundary point, and $H(\cdot)$ is the Heaviside step function.

– **Brownian force, $\boldsymbol{F_i^B}$**
This force deals with fluctuations due to thermal noise and it is modeled by a normal distribution with mean zero and standard deviation given by the fluctuation–dissipation theorem,

$$\boldsymbol{F}_i^{\boldsymbol{B}} = \sqrt{2\zeta k_B T}\frac{d\boldsymbol{W}_i}{dt}, \tag{5}$$

where each $\boldsymbol{W}_i = \left[W_{i,x}, W_{i,y}, W_{i,z}\right]$ is a 3D Brownian motion with statistics given by a standard normal distribution, with zero mean and variance satisfying,

$$\left\langle W_{i,p}\left(t\right), W_{j,q}(s)\right\rangle = \delta_{ij}\delta_{pq}\delta\left(t-s\right),$$

where $i, j = 1 \ldots N$ (number of particles) and $p, q \in \{x, y, z\}$.

2.2. Lessons learned from polymer bead–spring models of chromatin

2.2.1. Entropic fluctuations, excluded volume, tethering and confinement suffice to create first-order organization of chromosomes in the nucleus.

Studies of the dynamic behavior of chromatin fiber within the nucleus provide insight into how it explores nuclear space as well as the spatio-temporal interactions with functional molecules that are critical to DNA transactions [47,89,90]. Different studies have shown that the polymeric nature of chromosome arms alone can explain the leading order organization within the nucleus by generating domains of high intra-chromosomal interactions [65]. Fig. 3 shows that adding attractive potentials to a set of freely diffusing beads results in the formation of chains by giving rise to sites of preferential intra-chain interactions. On the other hand, the excluded volume potential, which mimics steric effects, reduces inter-chain interactions. Finally, the tethering of the chains not only helps to differentiate intra- and inter- chain interactions but also to explain the formation of chromosome territories as discussed in Section 2.2.2.

Modeling has also shown that the resulting contact maps not only depend on the bead–bead interaction potentials, but as

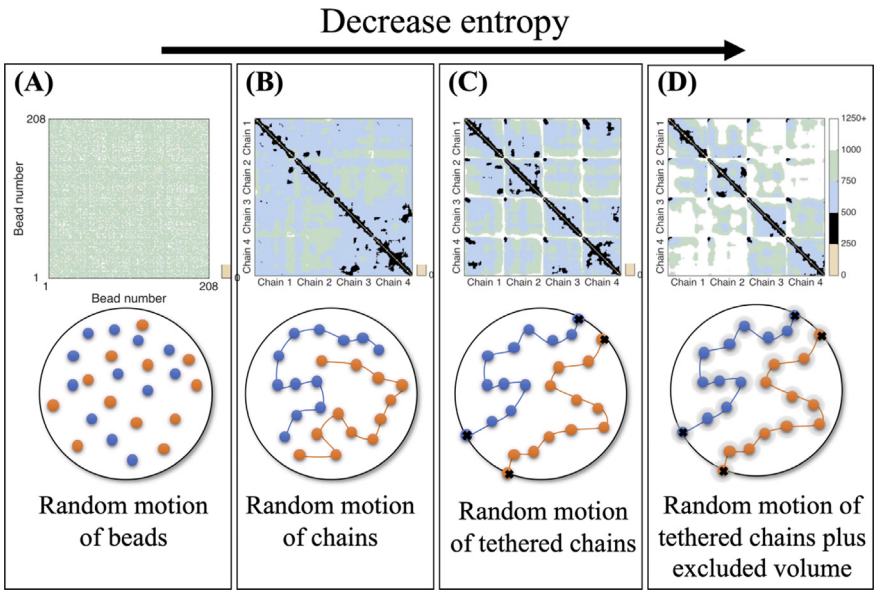

Fig. 3. Contact maps of averaged distances between beads in a 2D bead–spring model. The analysis of the distance between beads provides the means to make quantitative conclusions about contact and interaction dynamics of genes within and between different chromosomes. In the maps on the top row, the range of interactions represented by averaged separation between beads are binned according to distance (beige, 0–200 nm (nanometers); black 250–500 nm, etc.). (A) Beads confined to a circle of radius 1 μm and moving through Brownian motion. We start with the simplest approximation of 208 beads inside a circular domain (representing the nuclear envelope) moving via thermal fluctuations. The beads are independent of each other, meaning the only forces acting on the beads are the confinement force, viscous drag and Brownian forces; these last two are coupled according to the fluctuation–dissipation principle. Note the uniform distribution of beads separation (uniform green, 750–1000 nm) across the domain. (B) An attractive potential (wormlike chain spring law) is added to the same noise history as in (A). The addition of this potential allows the division of the 208 beads into 4 independent chains. Two chains (orange and blue) of the four chains are depicted in the cartoon. Comparison between the contact maps for (A) and (B) reveals the strong preference for each chain to self-associate (the black diagonal in (B), 250–500 nm separation). (C) Tethering of chains further decrease the degrees of freedom in the chain movement, causing a decrease in the entropy and further distinctions between intra- and inter chain interactions. Tethering is implemented through fixing the position of the end beads onto the boundary (black beads fixed at peripheral positions). This is a means to capture the biological tethering known to exist through centromere-spindle pole body interaction and telomere-nuclear envelope interactions. (D) Inter-molecular interactions are added to the same simulation through an excluded volume potential. This results in lower inter-chain interactions (off-diagonal blocks) and larger intra-chain interactions (main diagonal blocks).

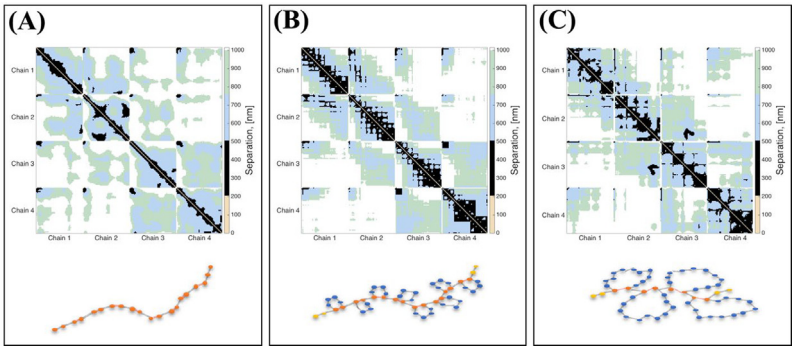

Fig. 4. Contact maps for different conformations that include loops and changes in the average distance between beads. Bead interactions are divided into backbone-to-backbone (orange-to orange), outer loop-to-outer loop (blue-to-blue) and backbone-to-outer loop (orange-to-blue). Intra-chain interactions are given by the main diagonal blocks of the contact maps, while inter-chain interactions correspond to off-diagonal blocks. The four chains are indicated on the *x*- and *y*-axes of the contact maps. The distances are binned according to the color scheme described in Fig. 3. (A) Linear, tethered chain conformation. The linear tethered chains are the same for Fig 3D and Fig. 4 A. (B) Loop conformation consisting of eight loops per chain, each loop comprising six beads. A major change comes from beads in the backbone of the same chain (more black regions in the main diagonal blocks), since loops in the chain bring backbone beads closer to each other. In addition, distances between beads in different chains increase (more white in the off-diagonal blocks). (C) Chains are organized into four loops per chain, each loop with 13 beads. In general, this new loop conformation has the same qualitative effect as the loops in (B): more smaller intra-chain distances and larger inter-chain distance. The main difference is observed in the intra-chain interactions as given by the black regions in the main diagonal of the contact maps. Larger loops in (C) result in a more fragmented intra-chain separation as compared to (B).

shown in Fig. 4, can also be modified by different chain configurations. In the nucleus the presence of different proteins and enzymes interacting with chromatin often results in the formation of loops within the fiber. Fig. 4 shows that chromosome interactions are also affected by the configuration of such loops and a direct consequence of this is that gene–gene interactions are also modified.

2.2.2. Centromere tethering confines chromosome domains and explains increase of mobility following DNA damage.

Computational studies in budding yeast have revealed that territorial organization of chromosomes is partially governed by chromosome tethering [54]. In yeast, the 32 telomeres (tether attachments of the chromosome ends to the nuclear envelope) from 16 chromosomes are clustered into four to six loci in the

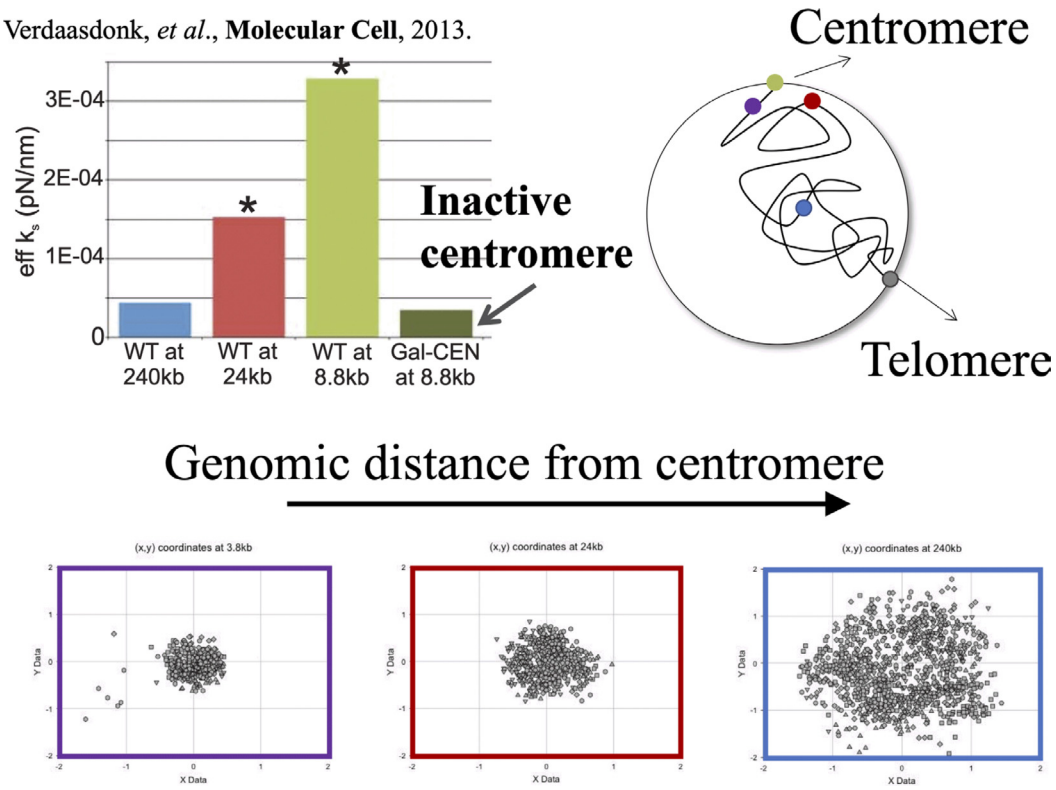

Fig. 5. Experimental measurements of loci motion as a function of distance from centromere (tethering point). Experimental measurements were taken from yeast cells containing fluorescent foci at specific locations along a chromosome as shown in Fig. 2C and in the schematic (Top right). In this situation, the chromosome is depicted as a single chain, tethered to nuclear periphery at two positions (the centromere and telomere). Two positions of the fluorescent markers are indicated. The orange spot is closer to the centromere 24 kb, while the blue spot is further from the centromere, 240 kb. Positional information for each spot was obtained over the course of approximately 10 min. The units on the *x*- and *y*-axes are in microns. Positional data was fitted assuming that each locus was connected to the centromere by a linear spring so that the bars in the top left represent effective spring constants. In the bottom scatter plots of loci positions are shown as a function of distance from the centromere from left to right. Closer to the tethering point (purple) movement is more restrictive, resulting in less variance in motion and higher (stiffer) spring constant. Farther from the tethering the loci increase its movement (red and blue); increased variance in motion results in lower (softer) spring constants. Mutant cells with a detached the centromere show an increase of motion of all loci, including those close to the centromere (dark green in bar plot, top-left).
Source: Figure from [54].

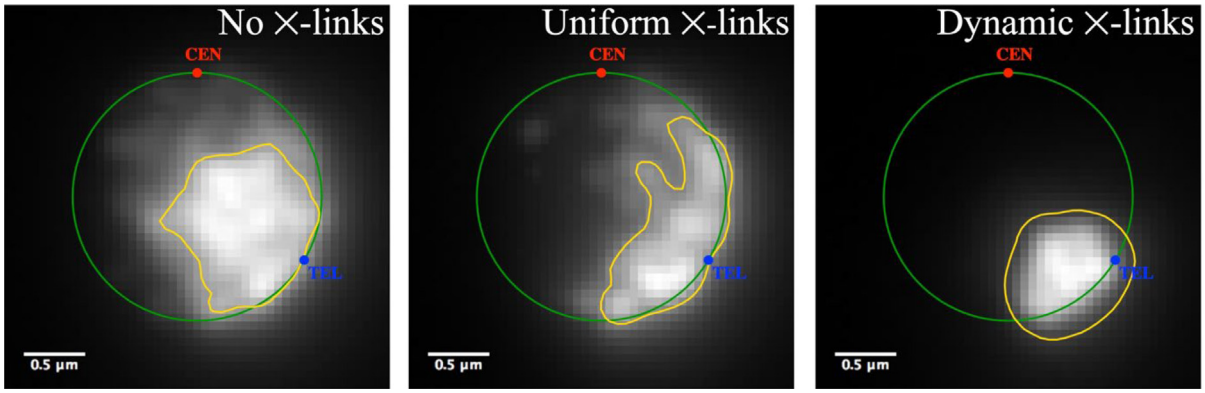

Fig. 6. In the cell nucleus polymer models have shown that the role of proteins is to guide, stabilize and sustain cycle- specific genome states. In order to compare the polymer model to experimental images of live cells, we utilize an experimentally derived point spread function (PSF) to generate a simulated 3D image from the model. A simulator module takes as input a 3D stack of images coming from a single fluorescent bead along with the x, y, z coordinates from the simulation and computes a maximum projection to create a single 2D image (shown above). In the model, protein interactions with the chromatin are captured via crosslinks and located at specific chromosome arms and beads to simulate the region within the nucleus (nucleolus) where there is a high concentration of cross-linkers between highly repeated ribosomal DNA genes in the nucleolus. Whether the crosslinks are present or not, or whether they are dynamic or static (uniform) directly affect the final configuration of the ribosomal DNA locus within the nucleolus.
Source: Figure adapted from [50].

nuclear boundary. Interior locations of all chromosomes, at specific sites along the chain for each, are commonly tethered at the centromere. These tethering loci constrain motion within the arm by reducing the degrees of freedom of both arms of each chromosome arm. Our polymer models and single cell experiments have shown that the magnitude of motion along each chromosome arm depends on bead position relative to the tether, either centromere or telomere. This is shown in Fig. 5 which

indicates that chromosome motion is constrained not only by the nuclear membrane itself, but also by the tethering of centromeres and telomeres to components in the membrane. Modeling [54] has further shown that experimental organization of chromosomes into territories (specific sub-volumes of the nucleus) can be replicated by tethering the bead–spring chains to the boundary, as shown in Fig. 2(B).

2.2.3. DNA damage-induced amplification of chromatin mobility

The fact that yeast chromosomes in vivo behave like polymers has allowed many aspects of chromosome architecture and chromatin movement to be reproduced in silico by bead–spring modeling. These findings have shed light into the understanding of cellular responses to DNA damage. In budding yeast, and human cells, after DNA damage an increase in chromatin mobility has been observed both at the sites where the lesions occur as well as at undamaged sites [54,74,91–96]. Enhanced motility has been attributed to both release of chromosomal tethers and histone degradation [54,93,96]. Both cases can be explained from polymer physics principles. As previously discussed, release of tethering results in an increase of the configurational degrees of freedom of a chain and as such in an increase of the modes of motion. Histone degradation can be related to a less-stiff spring constant in the model, and the fact that the chains are now composed of "floppy" springs results in an increase of the motion.

2.2.4. Emergent properties in chromatin organization, such as topologically associated domains (TADs), nuclear bodies, and phase separation of the nucleolus, coupled with clustering of genes, result from small molecule protein and enzyme "tuning" of chromosome conformations.

Chromatin structure is highly influenced by the action of Structural Maintenance of Chromosome (SMC) proteins, in particular condensin and cohesin [73,97,98]. The physical behavior of these proteins is only now becoming clarified and quantified, performing actions such as crosslinking within and between chromosomes and loop extrusion within chromosomes. The polymer model framework of chromatin provides a playground to explore the relationship between the microscale actions of these proteins and the resulting macroscale dynamic structure in the nucleus. Crosslinking action can be modeled by adding additional springs between pairs of beads that stochastically form (when they are within a prescribed distance) and break according to a prescribed mean timescale τ_{on}, which dictates the mean duration of a transient bond. To investigate phase separation in the nucleolus mediated by crosslinking, we added dynamic crosslinkers to the subset of beads within chromosome XII that comprise the nucleolus. Whether these crosslinkers are present or not, and whether they are dynamic or fixed, result in different configurations of the nucleolus, as shown in Fig. 6. In addition, even though the springs only connect pairs of beads, we observe that when τ_{on} is sufficiently small, such as around 0.1 s, this pairwise action leads to the formation of large, stable clusters of around 20 beads, and a clear phase separation of the nucleolus, as seen in Fig. 7. In contrast, when the timescale is slow, clusters do not form, and the nucleolus does not achieve the same level of compaction. The paradigm is again illustrated — weak, local crosslinking within segments of a large molecular weight polymer induces global emergent behavior, in this case both compaction and frequent, multi-scale, self-interactions. A subsequent study [49] explored a denser sampling of the crosslinking timescales, *discussed next*, whereby clustering within the nucleolus is further tuned by fast, but not too fast, crosslinking; this tuning of τ_{on} induces a transition from somewhat rigid to plastic clustering and mixing of clusters so that genes jump between semi-persistent clusters.

2.2.5. Complex emergent behavior is modulated by crosslinking dynamics

To paint a more detailed picture of the relationship between crosslinking timescales and dynamics, we can view the system in terms of waiting times for particular events, a standard technique in analysis of stochastic systems. We construct two waiting time statistics in terms of "interactions" of pairs of beads (which will be defined in two ways below). The first statistic represents the average time between the end of an interaction between a particular pair of beads and the next time they resume interacting, averaged over all occurrences of a pair of beads ceasing and then resuming interaction. The second statistic represents the average time between the beginning of an interaction between a particular pair of beads and the end of the interaction, averaged over all interacting events. Both statistics are further averaged over all pairs of beads and all timesteps. Fig. 8(A-B) shows both waiting time statistics for 2-point (i.e., bead pair) statistics, where two beads are defined as interacting whenever their pairwise separation is under a distance threshold of 100 μm. Fig. 8(C-D) generalizes both waiting times from gene pair interactions to the scale of clusters or communities computed with dynamic community detection algorithms [49], where two beads are defined as interacting at any timepoints where they are in the same community. Remarkably, we see that this first waiting time, which intuitively can be thought of as measuring the level of cross-communication between genes, at both the 2-point and community scales, is minimized over an intermediate – fast but not too fast – regime of crosslinking timescale, corresponding to maximum cross-communication at that timescale. One therefore finds that the 2-point structure statistics is the tip of the iceberg of a larger gene community scale organization. Furthermore, this non-monotonic behavior suggests that mixing in the genome, which is essential for biological processes such as homology search for repair of damaged chromatin, may be optimized by tuning the timescales of protein crosslinkers. Furthermore, the optimal timescale must be sufficiently broad, i.e., not a sharp valley, for biological robustness, which the model reflects in Fig. 8.

2.2.6. Dynamic network community detection tools provide automated identification of chromosomal structure on the spatial and temporal scales it exists

The development of a rich framework for studying chromatin dynamics and the effect of crosslinker-mediated interactions on the resulting dynamic structure necessitates corresponding development of analysis tools to agnostically detect and quantify results of the simulations. In particular, the emergence of a complex, dynamic clustering structure optimizing different attributes dependent on crosslinker timescale motivates a tool that can automatically identify clusters of beads over both space and time. This is challenging due to the requirement of balancing similarity over both space and time. By mapping the data into a multilayer network, this can be reframed as a dynamic network community detection problem Specifically, if at a particular time each pair of beads i and j are separated by a distance X_{ij}, we would define an adjacency matrix as

$$A_{ij} = \begin{cases} e^{-aX_{ij}} & X_{ij} < d^* \\ 0 & X_{ij} \geq d^* \end{cases} \tag{6}$$

Here d^* is a distance threshold for creating edges, and a is a parameter controlling how quickly edge weight decays with distance. We perform this process separately for a sequence of time points t_s, leading to a corresponding sequence of adjacency matrices A^s_{ij}. This sequence of adjacency matrices then defines a multilayer network, with layer s having adjacency matrix A^s_{ij}. Then, communities are identified using multilayer modularity

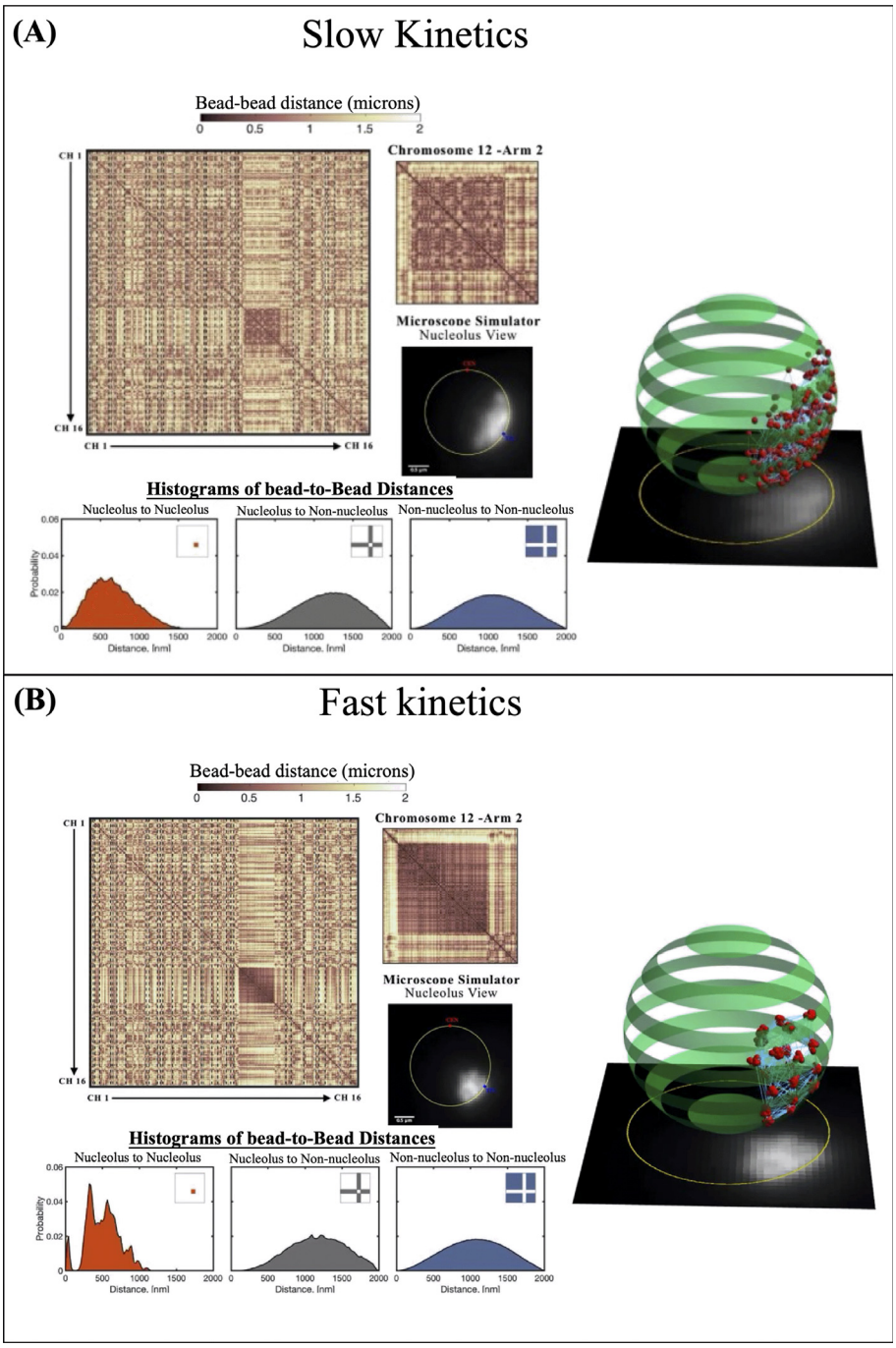

Fig. 7. Kinetic timescale of crosslinkers tunes distinct organizational phases in the nucleolus. Upper left: Contact maps showing a quantitative distribution of bead distances between the 16 chains (chromosomes) of yeast. The chains from 1 to 16, as indicated, are plotted on the *x*- and *y*-axes. Clustering of beads through cross-linking can be visualized as the dark brown square (shifted right and slightly below center) representing cross-links between the ribosomal RNA genes on chromosome 12. The inset (to right of contact map) shows a high magnification view of the clustered array. The positions of the cross-links are visualized through simulated fluorescence of the active beads on chromosome 12 (Microscope Simulator). Below the contact map histograms of bead distances are given. In red are histograms of cross-linking beads. These are active beads on chromosome 12 indicative of the cluster of ribosomal RNA genes in the nucleolus (labeled nucleolus to nucleolus distance). In gray are the distance distribution between nucleolar and non-nucleolar beads. In blue are the non-nucleolar to non-nucleolar bead distance distributions. To the right of the contact maps are snapshots from the 3D polymer model. The nucleus is shown as a sphere bounded by green bands. The cross-linkers and active beads are shown as red beads within the nucleus. The model is projected onto a 2D plane (described in Fig. 6) to simulate an experimental image. (A) With slow kinetics (mean crosslink duration greater than approximately 2 s) the nucleolus appears as a roughly homogeneous group of beads (red histogram), somewhat more compacted than the rest of the nucleus as visible in contact heatmaps. This manifests as the uniform distribution of red beads to the right. (B) When the crosslinking kinetics are fast (mean crosslink duration approximately 0.1 s), the beads condense into large clusters of ∼20 beads, causing a much greater degree of compaction than the slower kinetics, as visible in simulated microscope images. This clustering structure is also reflected in the bead-to-bead distance histogram within the nucleolus, showing distinctive spikes at characteristic inter-cluster distances (red histogram). This manifests as discrete clusters of red beads within the nucleolus shown to the right.
Source: Figure adapted from [50].

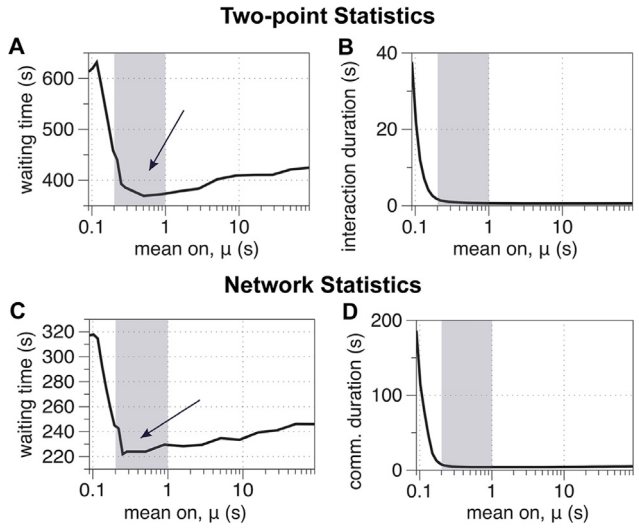

Fig. 8. The dynamic structure of the nucleolus can be characterized using waiting time statistics. Defining a two-point interaction as any pair of beads approaching within a distance of 100 μm, we compute waiting times between successive interactions (A) and waiting times for interactions from start to end (B) as functions of the mean persistence time for a bead–bead bond, where μ(s) in the figures is the same as τ_{on} in the discussion. The waiting time between successive interactions is minimized in the intermediate crosslinking regime (shaded + arrow), causing maximal mixing and cross-communication among genetic loci. Generalizing two-point interactions, we define a network interaction as two beads being in the same network community. We then compute the network interaction waiting time statistics in (C) and (D). We see remarkably similar behavior, revealing that two-point interaction metrics and statistics are a harbinger of a larger network interaction.
Source: Figure adapted from [49].

community detection, which seeks to optimize the modularity score

$$Q = \frac{1}{2M}\sum_{i,j,s,r}\left[\left(A^s_{ij} - \frac{\gamma k^s_i k^s_j}{2m_s}\right)\delta(s,r) + \omega\delta(i,j)\,C_{sr}\right]\delta\left(c_{is}, c_{jr}\right) \quad (7)$$

over the community labels c, where c_{ij} represents the label of bead i in layer s. Here, k^s_i is the degree of bead i in layer s, m_s is the total weight over layer s, $C_{sr} = \delta(s, r-1) + \delta(s, r+1)$, δ represents the Kronecker delta function, and $2M$ is a normalizing factor equal to the total multilayer edge weight. Intuitively, this metric measures how many more connections occur within communities in a layer than would be expected by chance, while also prioritizing beads that remain in the same community across layers. The spatial and temporal scales at which communities are identified can be tuned through the resolution and coupling parameters γ and ω, and *structure is considered meaningful when it is robust to variation in these parameters*. That the modularity score is linear in both of these parameters allows efficient identification of optimal partitions over a wide parameter space [99], and by choosing parameters in highly stable regions of the parameter space, we are able to use the data to identify the spatial and temporal scales at which the dynamic clustering structure exists.

The network framework expands the notion of two-point statistics to many-point statistics, by viewing a particular cluster of beads as an "interacting group or community". The significance of identified communities can be verified by confirming that implementing this network definition of interaction, (Fig. 8 C–D), remarkably reproduces the two-point interaction statistic (Fig. 8 A–B). Furthermore, the dynamic community detection algorithms identify, automatically, gene organization at the scale it exists, providing identification of gene organization and mixing between communities over time [49].

2.2.7. Quasi-potential theory mathematically confirms that weak linkers create structure through entropic fluctuation on an "effective energy landscape"

That many high-level behaviors of chromatin can be explained by entropic fluctuations suggests that the organization under SMC proteins might also behave like entropic fluctuations on an effective energy landscape, even though the random switching of the crosslinkers means that there is no true gradient potential of the force [49]. The local minimizers of an energy landscape, often called energy wells, predict the stable configurations (states) that a biological system is typically found in. Correspondingly, the heights of energy barriers between these wells predict how long it will take for a system to transition from one stable configuration to another, such that a higher energy barrier, or a deeper well, represents a state that the system is less likely to leave. On an energy landscape with potential energy $U(\vec{x})$, the long-time dynamics follow a Boltzmann distribution, with the probability density in terms of position $\vec{x}$ as:

$$p\left(\vec{x}\right) \propto e^{-U(\vec{x})/k_BT} \quad (8)$$

This motivates us to rewrite the dynamics of the beads in terms of a set of coupled Fokker–Planck equations, which model the time-evolution of the function $p_s\left(\vec{x}\right)$, representing the probability density that beads are in position $\vec{x}$ and the crosslinkers are in a bound configuration, which defines one of the switching states s [100]. These equations take the form

$$\frac{\partial p_s}{\partial t} = -\sum_{i=1}^{m}\frac{\partial}{\partial x_i}\left[v^s_i p_s\right] + \epsilon\sum_{i=1}^{m}\frac{\partial^2}{\partial x_i^2}\left[p_s\right] + \frac{1}{\epsilon}\sum_{k=1}^{n}S_{sk}p_k \quad (9)$$

over m total spatial dimensions (three per bead) and n total switching states. In the above, v^s_i represents all the forces on bead i in switching state s (i.e. crosslinker forces, effective confining wall forces), where ϵ is a parameter representing the size of fluctuations in the system and S_{sk} is a continuous-time Markov chain transition matrix representing the rate at which the system transitions from switching state s to k. Through a WKB-like ansatz in the small ϵ limit, this leads to an equation defining a *quasi-potential* $W(\vec{x})$ that effectively behaves as a potential defining a Boltzmann distribution and allows for energy landscape analysis. The gradient of this quasi-potential is defined as the value allowing for non-trivial solutions to the matrix equation $D(\nabla W) + A(x, \nabla W) + S(x) = 0$ where D is a diagonal matrix of the diffusion terms in (9), $D_{ss} = \sum_{i=1}^{m}\left(\frac{\partial W}{\partial x_i}\right)^2$, A is a diagonal matrix of the advection terms, $A_{ss} = \sum_{i=1}^{m} v^s_i\frac{\partial W}{\partial x_i}$, and S is the non-diagonal transition matrix. One interesting result from this approach is that randomly switching crosslinkers combine with Brownian motion to produce an effective energy barrier that is weaker than would be expected by a simple time average over the switching states, indicating that the model chromatin arm can more easily change configurations by utilizing the fluctuations in the switching crosslinkers. This quasi-potential theory can be applied to a variety of systems modeled by Brownian motion combined with randomly switching forces and poses an exciting avenue for future analysis of biological systems. The reader is referred to [101] for the details of this approach as well as additional references for quasi-potential and landscape theory.

3. Mucus in the human body: Modeling, rheology, and pathology

In the human body, mucus covers the luminal surface of the gastrointestinal (GI) [101], respiratory [102], and reproductive [103] tracts; mucus also coats the eyes, the epithelium of the nose, mouth, and salivary glands and the peritoneal surface of

intra-abdominal organs [104]. At the molecular level the underlying microstructure of all types of mucus is primarily composed of a "mucin polymer network". However, each organ-specific mucus barrier consists of distinct members of the mucin polymer family and are further biochemically tuned for diverse barrier and flow transport properties. Consequently, disease states are usually associated with a breakdown in the *normal* properties of the mucus barrier. While mucus is ubiquitous in the human body, and therefore fundamental to human health, the links between the molecular constituents of mucus, the mechanisms by which they are continuously replenished to maintain their critical functions, and the main microstructural features and variations of mucus throughout the body, remain active areas of research. Mucus functions as a viscoelastic, dynamic, semi-permeable barrier that protects organs and epithelial tissue by selectively trapping and discarding pathogens, toxins, and other particulates, or by maintaining a pH barrier in the intestinal tract [105]. Remarkably, while obstructing harmful particulates, mucus layers simultaneously allow the flux of water, gases, and nutrients that are transported through epithelial cells and distributed inside the body [104,106]. In performing these functions mucus is constantly secreted, shed, and digested, recycled or discarded. Given the fundamental role of mucus in human health, it is remarkable that many open questions remain regarding "healthy" organ-specific mucus and the pathways by which mucus becomes pathological. This knowledge is essential to guide approaches to treat or reverse pathology and has motivated 25 years of collaboration at UNC by Forest, Roberto Camassa, Rich McLaughlin, Sorin Mitran and many Ph.D. students and postdoctoral scholars with a host of interdisciplinary scientists from physics, chemistry, and medicine.

3.1. Mucus composition

A typical "healthy" human organ mucus sample consists of 90%–98% (by mass) of water, 2%–5% high molecular weight glycoproteins (mucins), 1%–2% lipids, 1% salts, and a small % of DNA fragments and other molecular species [107]. Mucus is generally classified as a physical gel whose quality derives primarily from mucins plus affinities to low molecular weight proteins that form a three-dimensional network or gel matrix [108–110]. The interlinking of mucins with other mucins and biomolecules creates the gel matrix. Among other things, the density and transient nature of crosslinks controls the characteristics of a gel network. However, other types of transient inter-molecular interactions of various characteristic time and length scales also contribute to the formation and strength of the mucus gel network. For comprehensive reviews on mucus gelation the reader is referred to [109,111–115]. As noted here, all mucus is not alike since the organs protected require completely different physical and chemical properties. Thus it is not surprising that the "mucin polymer family" is strikingly diverse and it has been argued that the mucin family is a misnomer and should be abandoned [116]. In our collaborations at UNC, we have focused on the mucus barrier in the human respiratory tract with colleagues in the Marsico Lung Institute and in the female cervicovaginal tract with the lab of Sam Lai on sexually transmitted viral diseases. The COVID-19 pandemic led us to merge our detailed understanding of respiratory mucus and antibody protection against mucus-coated epithelial tissue, focusing on inhaled respiratory viral infection and the essential role of the mucus barrier in the function of the immune system [24,26,27,117].

3.2. Mucus viscoelasticity

In general, mucus secretions are viscoelastic; however, their viscoelastic properties and responses vary significantly depending on the specific organ and function. For instance, Taylor et al. [120] showed that, in the stomach, two physically distinct mucus secretions are produced. One is a shear-resistant gel that forms a protective mechanical barrier and the other is a shear-compliant secretion, which transforms into a viscous liquid when subjected to even low mechanical shear stress and acts as a lubricant facilitating the movement of solid matter through the gut during the digestive processes. Intestinal mucus likewise must create a pH barrier to protect the epithelial tissue from the acidic environment necessary for food digestion. As is the case with other viscoelastic materials, the interplay between viscous and elastic properties directly affects the transport capabilities of mucus. However, other physical properties play an important role in the function of mucus. For instance, adhesiveness and wettability govern the properties of the interface between mucus and the epithelial surface [121]. Optimal conditions for the clearance and lubrication properties of mucus require that both wettability and adhesiveness are sufficiently high to prevent flow of mucus under body forces (e.g., no gravitational draining in the respiratory tract) while sufficiently low to propel mucus (e.g., via coordinated ciliary beating in the respiratory tract).

Although the mucin network primarily governs the rheological characteristics of mucus, other biochemical and external stimuli affect the properties of mucus by modifying gel formation and strength. Below we highlight examples where changes in rheological properties of mucus are induced by mechanisms not related to the self-dynamics of the mucin network.

- ***Human tears and lipids***. Rheological measurements of human tears reveal shear-thinning viscoelastic properties. Gouveia and Tiffany [122] showed that if the lipids in tears are removed, the fluid becomes Newtonian (shear-independent). This contrasts with other types of mucus where the mucin polymers impart non-Newtonian behavior.
- ***Gastric mucus and pH***. Dynamic light scattering and bulk rheology measurements reveal that gastric mucin solutions undergo a pH-dependent sol–gel transition from a viscoelastic solution at neutral pH ($\sim$7) to a soft viscoelastic gel in acidic conditions (pH $<$ 7), with the transition occurring near a pH of 4 [111,112].
- ***Airway mucus and salt***. Several studies showed that concentration of salts in mucin solutions changes their rheological properties [112,123,124].

3.3. Models for the rheology of human bronchial epithelial mucus

Significant insight into respiratory mucus has been gained from mucus harvested and reconstituted from human bronchial epithelial (HBE) cultures and then studied in the linear response regime by passive particle tracking microrheology [125–131] and in the nonlinear response regime by active magnetic microbead rheology [132–134]. What we learned about HBE mucus over the years is that it "yields" at incredibly low stress levels, and typical rheometers such as a cone-and-plate rheometer are not sensitive enough to impose 10 s of picoNewtons of frequency-dependent shear stress.

Such reconstituted samples from cultures serve as "model systems" for *in vivo* HBE mucus. The culture samples are harvested off the culture, dried, and then the solids consisting of mucin polymers and salts are reconstituted by adding water to a specified percentage by weight of solids wt%. In this way, we have been able to reconstitute HBE culture mucus to match

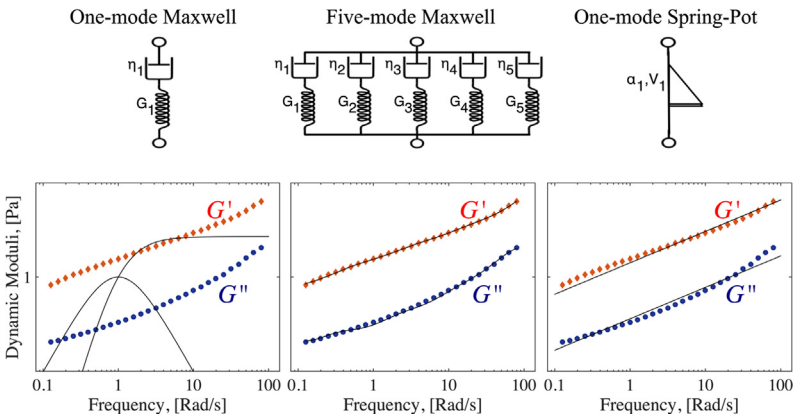

Fig. 9. Fittings of dynamic moduli from experimental data for 5 wt% HBE mucus to three models, where $G'(\omega)$ and $G''(\omega)$ represent, respectively, the frequency-dependent storage and loss moduli. *Left*: Upper Convected Maxwell (UCM) with one relaxation time (Eq. (10)), *middle:* UCM with five relaxation times (Eq. (11)), and *right:* spring-pot model (Eq. (12)).
Source: Data adapted from [118,119].

the wt% spanning normal ranges from healthy individuals to higher wt% associated with progressive disease, including cystic fibrosis, asthma, and COPD. The cultures can further be grown from HBE cells harvested from individuals with cystic fibrosis, a genetic disorder, or from healthy individuals without known genetic disorders. In early culture protocols for reconstitution of HBE mucus, the role of by-products of bronchial infection were not included, whereas infection is increasingly prevalent in progression of cystic fibrosis. The infection-free HBE mucus is a precursor to additional molecular species arising from infection, in particular much higher concentrations of DNA fragments, which are highly negatively charged just like mucins, plus positively charged molecular species. Indeed, these positively charged species provide the nucleating agents for mucin polymers to phase separate into insoluble, dense structures. In Section 4.5, we present a glimpse into how molecular dynamics modeling is reinforcing the experimental insights of mucus pathology [135].

Our early attempts modeled mucus using a 5-mode Upper Convected Maxwell (UCM) model [136]. The UCM model with one relaxation time has elastic and viscous moduli given by,

$$G'(\omega) = G_0 \frac{(\lambda\omega)^2}{1+(\lambda\omega)^2}, \qquad G''(\omega) = G_0 \frac{\lambda\omega}{1+(\lambda\omega)^2}, \tag{10}$$

where G' is the storage modulus, G'' the loss modulus and ω the frequency. The UCM model for each relaxation time is described by two parameters: G_0 is the plateau modulus, and λ is the relaxation time. The multimode UCM model consists of a linear superposition of single modes, each with a plateau modulus and relaxation time, and the moduli are given by

$$G'(\omega) = \sum_i G_{0,i} \frac{(\lambda_i\omega)^2}{1+(\lambda_i\omega)^2}, \qquad G''(\omega) = \sum_i G_{0,i} \frac{\lambda_i\omega}{1+(\lambda_i\omega)^2}. \tag{11}$$

Fig. 9 shows fittings to a reconstituted 5 wt% HBE culture sample. The fact that more than one UCM mode is necessary to fit the data indicates the presence of a spectrum of relaxation modes, and furthermore there must be some scaling law of the relaxation spectrum that underlies the power law structure observed. We return to this remarkable property of HBE mucus rheology below. In addition, the fact that the storage modulus is larger than the loss modulus indicates that 5 wt% HBE mucus is a solid-like "gel" at the experimentally accessible frequencies. This is in contrast to mucus of lower concentration where typically $G'' > G'$, defined as a liquid-like "sol" phase. The concentration at which the transition from a sol to a gel is called the gel point (GP). Studies have shown that the GP for reconstituted HBE mucus is in the range of 3–4 wt% [118].

The power law behavior observed in mucus data is the result of a wide range of microstructural length and time scales. Another coarse-grained option that has received attention in the stochastic process community in recent years is the use of fractional calculus in constitutive modeling of power-law fluids. The main reason is that fractional models can describe simply and elegantly the complex characteristics of these viscoelastic materials. The simplest class of fractional models, the fractional element or spring-pot was introduced by Scott Blair [137], its constitutive equation can be expressed as

$$\sigma = V \frac{d^\alpha \gamma}{dt^\alpha}, \tag{12}$$

where V is a material-dependent constant, σ is the stress and γ represents the strain. It follows that the dynamic moduli for the spring-pot model both follow a power law in the frequency domain $G' \sim G'' \sim \omega^\alpha$. Fitting of mucus data to a spring-pot model is shown in Fig. 9. However, such models are not rooted in fundamental polymer physics. In a completely different approach to modeling of power-law complex fluids, in [138] we extended the classical statistical physics, generalized Langevin equation (GLE) models of Rouse and Zimm, respectively. The Rouse and Zimm models exhibit transient anomalous diffusion, and exhibit power law scaling of $\alpha = 1/2, 2/3$, respectively, within a wide intermediate range of timescales that encompass experimental measurement timescales. There is a subtle mathematical correspondence at play here, explained in [138,139], between the ensemble averaged mean-squared displacements (MSD) of the polymer medium, the MSD of the time series increments of micro-scale passive particles within the medium, and the remarkable fact that the Fourier transform of a power law function preserves the power law in the frequency domain. Thus, for each individual tracked bead, a power law MSD translates to a power law in the dynamic moduli of the medium surrounding that bead. We return to the relevance of this observation in Section 4.4. In [138], we generalized the Rouse and Zimm models to capture any sub-diffusive exponent α between 0 and 1, valid within the timescales of memory of the complex fluid, while beyond the longest memory timescale the MSD and therefore the dynamic moduli converge to simple viscous scaling, as with the special Rouse and Zimm kernels. We thereby provided a model basis for all power-law transient subdiffusive processes to apply to experimental data on respiratory mucus. Subdiffusive behavior is usually associated with (i) beads or other

passive microscale probes moving through a viscoelastic medium, (ii) binding/unbinding of the beads with other molecules in the medium and/or (iii) obstructed motion [140]. For viscoelastic materials exhibiting a power law behavior of the viscous and elastic moduli with respect to time, $G'', G' \sim t^{\beta}$, there is a direct correlation between subdiffusion within the material and its viscoelastic properties. For other viscoelastic materials, anomalous diffusion is still linked with viscoelasticity, however the relation between these two domains is not as straightforward to determine.

4. Diffusion of particles in HBE mucus to infer linear viscoelastic moduli plus molecular dynamics simulations: Healthy and pathological HBE mucus

The trapping and clearance of inhaled particulates in respiratory mucus layers has been studied for decades [141]. Above a particle diameter relative to the mucin polymer network, particle diffusion within the mucus barrier is not a simple process where particles obey Brownian diffusion laws; the mucin polymers in salt water plus other molecular species create a network whose fluctuations are both dissipative and elastic. Embedded micron-scale particles are not simply bombarded by water molecules, instead they exhibit memory in the increments from thermal fluctuations of the polymer network. Experimental tracking methods have provided a wealth of data on particles with diameters between tens of nm and several microns, where the particles not only range in size (hydrodynamic radius) but also in their surface interactions with the mucin gel network. The study of self-diffusion of nm-to-micron scale particles in mucus is not only a means to determine the equilibrium viscous and elastic moduli versus frequency, but furthermore important to determine the movement of toxic particulates within mucus, as well as for inhaled drug delivery and gene delivery therapies [35,106,142].

The heterogeneous, three-dimensional network formed by mucins in mucus can be viewed as a physical obstruction to particle diffusion. This effect is modeled as a reduced self-diffusion coefficient of the particles. We can understand this by considering the ensemble-averaged, mean-squared displacement (MSD), $\left\langle \Delta r^2\left(n\tau\right)\right\rangle$, of tracked particle position time series, defined as

$$MSD_X\left(n\tau\right) = \frac{1}{N-n+1}\sum_{i=0}^{N-n}\left\|\boldsymbol{X}_{n+i}-\boldsymbol{X}_i\right\|^2, \tag{13}$$

$$\left\langle \Delta r^2\left(n\tau\right)\right\rangle = \frac{1}{N_p}\sum_{p=1}^{N_p} MSD_{X_p}(n\tau),$$

here N_p is the number of particles, N is the total number of measured increments for each particle path, n is the number of experimental frames, and τ is the experimental lag time between recorded positions of the microscope. Reported values of MSD in mucus [118,141,143–145] reveal a sub-diffusive MSD scaling over an intermediate dynamic range of lag times for each individual tracked particle position X_{p},

$$MSD_{X_p}(n\tau) \sim D_a(n\tau)^{\alpha}, \tag{14}$$

where $0 < \alpha < 1$. The pre-factor D_a is a *generalized diffusion coefficient*, and instead of the usual units of $\mathrm{L}^2\ \mathrm{t}^{-1}$ for diffusion coefficients, it has fractional units of $\mathrm{L}^2\ \mathrm{t}^{-\alpha}$. The appearance of fractional units requires care in analysis since all tracked beads have different α and therefore there is no quantitative comparison of multiple beads based on D_a, which we address below. When microscopy experiments are performed for sufficiently long times, a transition to linear scaling of the diffusion constant $D_a\ (\alpha = 1)$ appears, yet only beyond the longest memory timescale of the medium. We rarely track long enough to see the transition from sub-diffusive to diffusive scaling, so that all experimental lag times of individual tracked beads exhibit power law scaling. For direct modeling of tracer particles in a viscoelastic medium, a sufficiently robust family of stochastic processes is needed that reflects these fundamental MSD signatures of transient sub-diffusion. Below we summarize two models that have been successfully used to describe diffusion of particles in mucus; first we recall simple Brownian motion.

4.1. Brownian motion

The equation of motion describing the velocity of a particle driven by Brownian motion is given by the Langevin equation,

$$m\frac{d\boldsymbol{v}}{dt} = -\zeta\,\boldsymbol{v} + \boldsymbol{F}\left(t\right), \tag{15}$$

where $\boldsymbol{v}$ is the velocity of a Brownian particle with mass m and drag coefficient ζ. The force $\boldsymbol{F}\left(t\right)$ comes from random fluctuations and is assumed to be white noise, i.e.,

$$\begin{aligned}&\left\langle \boldsymbol{F}\left(t\right)\right\rangle = 0,\\ &\left\langle \boldsymbol{F}\left(t\right)\boldsymbol{F}\left(s\right)\right\rangle = 2\zeta k_B T\delta\left(t-s\right)\end{aligned} \tag{16}$$

here k_B is the Boltzmann constant and T the absolute temperature, and $\langle\cdot\rangle$ gives the ensemble average. In the zero-mass limit, the particle position can be found as,

$$\zeta\frac{d\boldsymbol{X}}{dt} = \boldsymbol{F}\left(t\right). \tag{17}$$

It follows that the MSD of a particle undergoing Brownian motion is $\left\langle \Delta r^2\left(\tau\right)\right\rangle \sim \tau$.

4.2. Fractional Brownian motion (fBm)

Fractional Brownian motion (fBm) is a self-similar Gaussian process with stationary increments and an *exact, uniform MSD scaling behavior*, for all lag times $n\tau$ [146]

$$MSD_X(n\tau) = D_{\alpha}(n\tau)^{\alpha}, \tag{18}$$

where D_{α} is the generalized diffusion coefficient, defined above. The autocorrelation function for fBm is likewise exactly known, and given by

$$E\left[B_{\alpha}\left(t\right)B_{\alpha}\left(s\right)\right] = \frac{1}{2}\left(|t|^{\alpha}+|s|^{\alpha}-|t-s|^{\alpha}\right), \tag{19}$$

where $B_{\alpha}\left(t\right)$ is a 'reduced fractional Brownian motion' with parameter α. For a more detailed discussion of $B_{\alpha}\left(t\right)$ the reader is referred to [146].

Long-range correlations are given by

$$\left\langle \xi_{\alpha}\left(0\right)\xi_{\alpha}\left(t\right)\right\rangle \approx \alpha\left(\alpha-1\right)t^{\alpha-2}, \tag{20}$$

where ξ_{α} is the fractional Gaussian noise, $\xi_{\alpha}\left(t\right)$, which is the appropriately defined derivative of $B_{\alpha}\left(t\right)$, the details of which we refer again to [146] and references therein. Uncorrelated Brownian motion corresponds to $\alpha = 1$. For $0 < \alpha < 1$ the increments are negatively correlated, rendering the associated process sub-diffusive. Conversely, when $\alpha > 1$ the motion is persistent (positively correlated), resulting in super-diffusion in which successive steps are biased to follow in the same direction.

The Langevin equation describing fBm can then be written as

$$\zeta\frac{d\boldsymbol{X}}{dt} = \xi_{\alpha}\left(t\right), \tag{21}$$

where $\boldsymbol{X}$ represents the bead position.

Fractional Brownian motion has been used to model a wide range of processes including monomer diffusion in a polymer chain [147], polymer translocation [148], diffusion of biopolymers

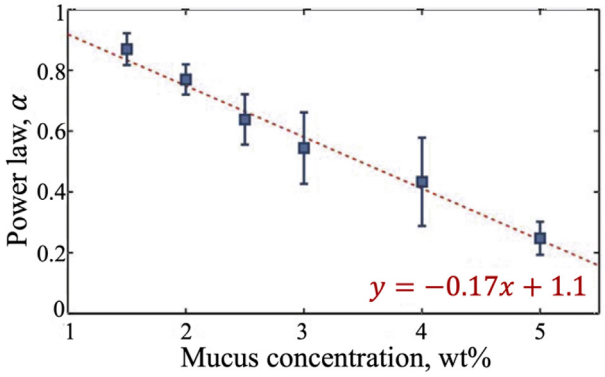

Fig. 10. Power law representation of the sub-diffusive exponent a versus wt% solids of HBE mucus, computed from passive particle tracking microrheology. The fittings are obtained by assuming that the diffusion of probes in the mucus sample has a mean square displacement (MSD) that follows a power law with respect to experimental lag time (τ), $MSD \sim \tau^{\alpha}$.
Source: Adapted from [118].

inside cells [149], bacteria chromosomal loci [150], diffusion in crowded fluids [151], and diffusion of passive microbeads in HBE mucus [118].

Related to mucus, Hill et al. [118] found for different reconstituted HBE mucus concentrations and over experimental time scales (1/60–30 s), that single particle and ensemble MSD data were remarkably well approximated by a uniform power law, and therefore consistent with a scaling given by Eq. (18). Furthermore, as shown in Fig. 10, the power law exponent α is well described by linear function of mucus concentration.

4.3. fBm as a classifier of particle-tracking data in human bronchial epithelial mucus

In this and the next two subsections we focus on a series of new challenges in passive particle-tracking microrheology of *pathological mucus, marked by extreme heterogeneity, that develops during progression of cystic fibrosis* (CF) [126,152–155]. We summarize highlights from ongoing, unpublished work to be submitted, [135], without compromising the novelty therein. We present these highlights to underscore that even after 25 years of the UNC Virtual Lung Project, new experimental, clinical, and mathematical advances continue to advance our understanding of lung biology and medicine.

Specifically, mucus undergoes a heterogeneous phase transition: dense, raft-like, structures, referred to as *flakes*, self-assemble, and phase separate from the remaining more dilute solution. In advanced stages of CF [155], up to 50% of the mucin polymers (MUC5B and MUC5AC) comprise the flakes that do not swell nor dissolve in airway surface salt-water solvent. Advanced CF mucus is thereby, at a coarse scale, a two-phase mixture: a dense phase of mucin flakes and a more dilute phase of the remaining mucins in solution. Additional heterogeneity potentially exists, especially the free-volume pore distributions within phase-separated flake structures.

Probes are mixed in the reconstituted HBE samples with flakes and allowed to sit overnight. When probes enter flakes, their diffusive mobility is low, sometimes sufficiently low to be indistinguishable from immobile probes tracked by the instrumentation. Heterogeneity, low bead sample sizes, and unknown sampling efficacy of the heterogeneous domains combine to impose hard constraints on the form of the Generalized Stokes–Einstein Relation (GSER) one should use, and to limit inference of rheology due to low realization numbers. Ensemble averaging of MSDs in the GSER is justified by an ergodicity assumption for homogeneous materials: ensemble averaging of MSDs in the time domain is equivalent to frequency-domain averaging of the Fourier-transformed MSDs, further assuming the beads give a sufficient random sampling of the material. These assumptions are strongly violated for flake-prevalent mucus.

For all data distinguishable from the noise floor, we extract the pure entropic fluctuation signal using the *fractional autoregressive moving average* (fARMA) denoising model developed in Ling et al. [154]. The success of the fARMA denoising procedure is sensitive to the initial value in the nonlinear optimization procedure, accordingly we introduce a predictor–corrector method to ensure a stable initial condition in [139]. The predictor–corrector method yields a 2-parameter classifier of the purely entropic, medium-induced, sub-diffusive MSD over measured timescales.

It is important to emphasize that the statistical classifier for Brownian motion is one-dimensional, the diffusivity D, whereas *for sub-diffusive fractional Brownian motion, the classifier is two-dimensional,* (α, D_α). The power law α reflects the degree of sub-diffusivity of the medium surrounding each tracked particle. As noted above, the pre-factor D_α has α-dependent units, so that *one cannot compare numerical values of different beads* unless they have identical α, *nor can one perform arithmetic operations (e.g., averaging) over ensembles of tracked particles*. Moreover, one cannot employ clustering metrics. Therefore, to determine heterogeneity of each HBE sample from the primitive, measured MSD data of the ensemble, we use a non-dimensional version of D_α, which we label $\widetilde{D}_\alpha$. In this way each probe is assigned a 2-parameter, dimensionless metric of mobility, $(\alpha, \widetilde{D}_\alpha)$. To render the pre-factor dimensionless, using only experimental scales and a reference fluid relevant to mucus, we define a rescaling of D_{fBm} which depends on the power law α, spatial dimension d, and particle radius r and normalize with respect to the corresponding diffusivity in water, D_w,

$$\widetilde{D}_\alpha = \frac{d^{2(\alpha-1)} D_\alpha}{(D_w)^\alpha}. \tag{22}$$

Here $D_w = \frac{k_B T}{6\pi\eta_w r}$, where water viscosity is $\eta_w = 1$ mPa-s.

The most common method (cf. [118,126,152]) for estimating the classifier parameters (α, D_α) is via a least-squares (LS) method, which consists of fitting the slope and intercept in the relation

$$\log\left(MSD_X\left(n\tau\right)\right) = \log\left(2dD_\alpha\right) + \alpha \cdot \log\left(n\tau\right). \tag{23}$$

It is known that the empirical MSD is contaminated by noise at both the smallest and largest timescales, for this reason only lag-times $n\tau$ in a restricted bandwidth are often used. This approach does not remove the noise from the selected bandwidth; it merely assumes that noise contamination is negligible therein. However, this assumption is violated when the particle's mobility (i.e., the signal of interest) is close to the noise floor, the precise low signal-to-noise regime that arises in pathological "flake-burdened" mucus from progressive cystic fibrosis.

To illustrate this, Fig. 11a displays the MSD of fBm contaminated by a noise floor of magnitude σ^2, for which the MSD is given by

$$MSD_{fbm+noise}\left(t\right) = 2dD \cdot t^\alpha + 4 \cdot \sigma^2 \tag{24}$$

LS fitting is done within the 0.1–2 s bandwidth, and the line of best fit agrees very well with that of the empirical MSD over the bandwidth. However, this fit is to the MSD consisting of signal plus noise: Fig. 11b shows that the LS fit greatly diverges from the MSD of the pure signal. In contrast, an extension (introduced next) of the fARMA denoising method of Ling et al. [154] accurately recovers the pure signal in low signal-to-noise ratio (SNR) data, Fig. 11b.

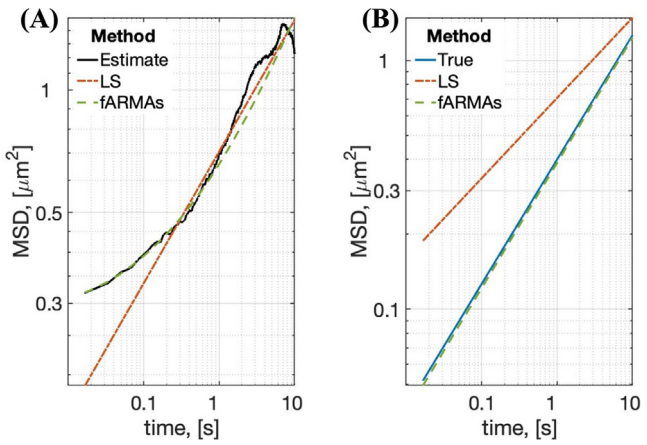

Fig. 11. (A) From selected from experimental data, plots of the empirical ("Estimate" in the figure) and fitted MSDs using the traditional least-squares method (LS) and the fARMAs method developed in [139] and explained in the text. (B) From selected simulated data of fractional Brownian motion with noise, LS and fARMAs estimates of MSD compared to the "true" signal.

4.4. The fARMAs denoising method for extracting the signal in low SNR data

For ease of presentation, we describe the method for a one-dimensional particle trajectory X(t). For extension to d > 1 dimensions, see [154]. The fARMA model assumes that X(t) is fractional Brownian motion with linear drift, μ,

$$X(t) = \mu t + \sqrt{2D_\alpha} B_\alpha(t). \tag{25}$$

However, we observe not $X(t)$ but rather $Y_0, \ldots, Y_N$, corresponding to noisy measurements of $X_n = X(n \cdot \tau)$, from which we develop a method to back out the pure entropic fluctuation signal, which we approximate in terms of fBm. This approach to signal extraction was first proposed by Savin and Doyle [156], who used the measurement model

$$Y_n = \widetilde{X}_n + \epsilon_n, \qquad \widetilde{X}_n = \frac{1}{\tau}\int_0^\tau X(n \cdot \Delta t - s)\, ds, \tag{26}$$

where ϵ_n is white noise with representing "static" localization errors, and $\widetilde{X}_n$ represents "dynamic" errors due to motion of the particle during the camera aperture time τ. Static errors have the effect of raising the MSD of Y relative to that of X at the shortest timescales, whereas dynamic errors have the opposite effect. While theoretically appealing, Ling et al. [154] found the Savin–Doyle model lacking in flexibility to account for the complex interactions between signal and noise from one experimental setup to another. Instead, they propose an ARMA + noise floor model of the form

$$\begin{aligned} Y_n &= \widetilde{X}_n + \epsilon_n, \\ \widetilde{X}_n &= \theta\widetilde{X}_{n-1} + (1-\theta-\rho)\,\widetilde{X}_n + \rho\widetilde{X}_{n-1}, \end{aligned} \tag{27}$$

where θ and ρ are the fitting parameters of ARMA. Specifically, the model of Ling et al. [154] does not contain the static noise term ϵ_n, but in [139] we show this term improves the model fit for in-flake particles that are distinguishable from the noise floor. We refer to the model (27) as fARMAs due to the addition of static noise.

Ling et al. [154] provide a computationally efficient method of fitting the fARMA model parameters $\Theta = (\alpha, D_\alpha, \mu, \theta, \rho)$ using maximum likelihood estimation (MLE). However the MLE requires numerical optimization of the likelihood function, which as noted above we found to be highly sensitive to the choice of initial value with low SNR data from particles in flakes. To address this, we implemented a predictor–corrector algorithm [139]: the predictor step is the LS estimate of (α, D_α), providing stable initial data for fARMA as the corrector, and the addition of one additional fitting parameter, s, the standard deviation of the static noise ϵ_n.

4.5. Molecular dynamics simulations of flake-burdened mucus

As a gel-forming polymer, it is natural to study mucus via molecular dynamics simulations, previously in [113,131,135,157], by our group more recently [158] and currently [135]. Our purpose in [158] was to capture detailed local hydrophobic and electrostatic domain interactions between polymer domains in order to understand how mucus hydration in progressive cystic fibrosis might, by itself, create closer proximity between the local hydrophobic and electrostatic domains. As a result, the charge interactions are effectively amplified by higher mucin concentrations in dehydrated conditions. In work in preparation [135], we extend the molecular dynamics framework in [158] based on chemical evidence that the hydrophobic termini of mucins are more accurately modeled using a Born–Mayer–Huggins (BMH) potential, which has a shorter interaction range with a deeper potential well than the 'standard' Lennard-Jones (LJ) potential [159] used in [158]. Using the LJ potential in the brush domains and the BMH potential in the termini domains and the HOOMD molecular dynamics platform [160], larger systems can be simulated for longer times than in [158].

Briefly, each mucin polymer (5 μm long) is comprised of a repeat of mucin monomers (500 nm long), and as in [158] we use the chemical structure of the primary gel-forming mucin in human bronchial epithelial mucus, MUC5B. The end termini of each monomer are highly hydrophobic with an internal region of glycosylated, brush domains that experience electrostatic interactions, and cysteine knots that are sparse and do not play a significant role in our simulations. We coarse grain this structure by choosing a characteristic bead size (σ) of 9 nm for the simulation to approximate both the size of the glycosylated brush and the persistence length of the MUC5B polymer. Simulations are run at 37 C (1 k_BT = 4.282E−21 J). For the details of converting between physical and simulation units, refer to the seminal paper by Kremer and Grest [161], or to [158]. Each mucin polymer then consists of 570 beads to resolve the mean molecular weight of MUC5B, with hydrophobic regions where the monomers are attached to each other and separated regions of cysteine knots and glycan brush regions [158]. Introducing a more realistic hydrophobic potential requires two new parameters: the depth of the hydrophobic potential, and the screening length of electrostatic interactions between brush domain beads. The Debye length (screening length) in mucus is around 1 nm, consistent with the ionic environment. All non-bonded pairs of beads experience pair-wise interactions depending on their type, with excluded volume interactions to prevent steric overlap, hydrophobic interactions for the termini, and electrostatic interactions via a Lennard-Jones potential for the glycosylated brush regions. Excluded volume interactions between non-bonded pairs are implemented via the Weeks–Chandler–Andersen (WCA) potential

$$U(r)_{WCA} = \begin{cases} 4\epsilon\left[\left(\frac{\sigma}{r}\right)^{12} - \left(\frac{\sigma}{r}\right)^{6}\right] + \epsilon & , r < 2^{\frac{1}{6}}\sigma, \\ 0, r \geq 2^{\frac{1}{6}}\sigma, \end{cases} \tag{28}$$

where r is the separation between the beads, σ is the bead size, and ϵ is the strength of the potential. This potential is purely repulsive. Hydrophobic interactions are implemented via the Born–Mayer–Huggins (BMH) potential

$$U(r)_{BMH} = Ae^{(\sigma - r)/\rho} - Cr^{-6} + Dr^{-8}, r < 2.5\sigma, \tag{29}$$

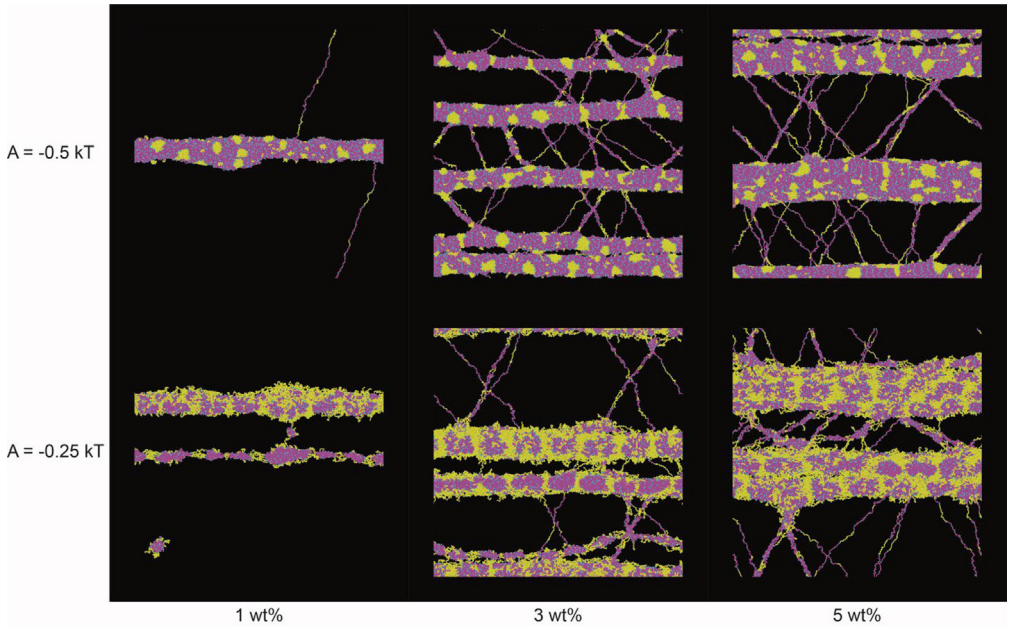

Fig. 12. The quasi-equilibrium structure, via molecular dynamics simulations, of 1, 3, and 5 wt% MUC5B "pathological mucus". Here we show 2D projections of the final simulation state (at 500,000 timesteps), with electrostatic beads representing the polymer brush regions in magenta, cysteine knots in cyan, and hydrophobic termini in yellow. The strength of the electrostatic (Lennard-Jones) potential is set at 1 kT for all images, while the strength of the hydrophobic (Born–Mayer–Huggins) potential changes along the *y*-axis. Simulation box size is 1800 nm on a side.

in which ρ is the screening (Debye) length, and C and D control the Lennard-Jones-like behavior of the potential ($C = 1\ k_BT\ \sigma^6$, $D = 1\ k_BT\ \sigma^8$). Finally, the electrostatic interactions are implemented via a standard Lennard-Jones (LJ)-like potential

$$U(r)_{LJ} = \begin{cases} 4\epsilon\left[\left(\frac{\sigma}{r}\right)^{12} - \left(\frac{\sigma}{r}\right)^{6}\right] + \epsilon & , r < 2.5\sigma, \\ 0, r \geq 2.5\sigma, \end{cases} \tag{30}$$

where the terms and cutoff are set differently than the WCA potential. Adjacent beads (those that are bonded to each other in a single polymer chain) are held together with the finitely extensible nonlinear elastic (FENE) bond potential

$$U(r)_{FENE} = -0.5KR_0^2 ln\left[1 - \left(\frac{r}{R_0}\right)^2\right] + 4\epsilon\left[\left(\frac{\sigma}{r}\right)^{12} - \left(\frac{\sigma}{r}\right)^{6}\right] + \epsilon, \tag{31}$$

in which $K = 30.0\ k_B\ T\sigma^2$, $R_0 = 1.5\sigma$, $\epsilon = 1\ k_BT$, and σ is the characteristic distance of the system (in this case 9 nm) [161]. The first term (spring-like force) is enforced up to R_0. The last set of terms is the same as the WCA potential to enforce excluded volume interactions between bonded beads, using the same cutoff $r \geq 2^{\frac{1}{6}}\sigma$. (For this review, we opt not to insert the multiple conditions on r within Eq. (31), which will be detailed in a forthcoming study [135].) Integration is carried out using the Langevin thermostat with unit drag for all particles in the system to implicitly represent the solvent [162].

HOOMD-blue allows simulations of larger systems for longer times using a GPU architecture. Aside from having to implement the BMH potential as a HOOMD pair interaction, all other potentials and configurations of the system were implemented using out-of-the-box HOOMD and Python. Each simulation was carried out for 500,000 τ (roughly 285 μs) in cubes of side length 200 σ (1800 nm). Weight percentage of mucus was derived assuming that mucus/mucin proteins have the same density as other proteins and are immersed in water.

In [135], we explore a wide range of mucin weight percentage, electrostatic interaction strength, and hydrophobic interaction strength. In Fig. 12, we simply show the results of quasi-equilibrium structures, visibly resembling experimental micrographs of the flakes discussed earlier, that arise at 1, 3, 5 wt% MUC5B "pathological mucus". Here we have imposed conditions in the simulations that instantiate the solvent pathology that arises from prevalent lung infections in cystic fibrosis. Namely, in normal solvent conditions the negatively charged, glycosylated interior brush domains of MUC5B experience repulsive electrostatic interactions. However, positively charged molecular by-products of infection reverse the interactions by inserting third-party intermediates that co-bind the brush domains. This is modeled in all simulations in Fig. 12 by fixing the electrostatic, Lennard-Jones potential strength at 1 k_BT. Then we further tune the strength of the hydrophobic, BMH potential, at 0.5 k_BT (top row) and 0.25 k_BT (bottom row), for each of the progressively higher 1, 3, 5 wt% MUC5B. These choices each yield structures consisting of rope-like entangled MUC5B polymers as the primary structural component. The 1 wt% structure is a condensed MUC5B rope, then the 3 wt% structure forms a network of ropes connected by thinner MUC5B strings, then the 5 wt% structure consists of thicker ropes in a connected network. More details of the chemical constituents that underlie both of these electrostatic and hydrophobic potential strengths are presented in [135].

5. Conclusion

We have highlighted several examples of a biological paradigm underlying emergent behavior. In this paradigm, spatially distributed and pervasive local, weak transient interactions, both within and between typically large molecular weight biological polymers, lead to functionality at much larger spatial and temporal scales. The multi-scale details of these systems continue to be studied, both in health and disease, with the aspiration that with sufficient understanding it will be possible to treat, reverse, or in some cases, prevent pathology. We conclude with a look forward on the two biological systems we have covered in this review article, chromosomal DNA and respiratory mucus.

The ability of cells to access genetic information relies in part on the spatial organization of chromosomes within the nucleus.

Major strides in understanding higher-order structures (beyond nucleosomes) have come from the discovery of loop-extruding and cross-linking properties of the class of structural maintenance of chromosome proteins. Equally impactful is the realization that the physical properties of the substrate, i.e., chromatin itself, contribute to the structural organization. The multiple modes of chromatin modification together with cross-linkers and loop extrusion capability result in a staggering degree of variation in loop size and distribution. We are just beginning to realize the power of chromatin loops to dictate biological function. The size and density of loops are responsible for the ability of cells to use tension-sensing mechanisms to achieve high-fidelity chromosome segregation [64,73,163]. DNA loops provide the means to condense chromosomes in mitosis [164] and provide the structural platform for high-throughput ribosomal gene transcription in the nucleolus [50,165,166]. Through the analysis of how variations in loops scale with different physical properties of the chromatin and condensin, it is anticipated that we will soon demystify the heterogeneity and dynamics observed in live cells across phylogeny.

In cells, how these loops participate in sequestering biochemical activities through their topological control and/or the spatial proximity of the looped sequences remains to be determined. The distributions of loops in vivo, unlike the thermal physics-based model presented here, are decidedly not randomly distributed, but rather exhibit cell-type and cell-cycle-specific patterns. Together with the major drivers of loop size and distribution (i.e., cross-linking proteins such as condensin), the stiffness of the chromatin and internal tethers such as entanglements that anchor regions of chromatin must interact and feedback on one another in biologically relevant ways. It is likely that all of these dynamic activities are subject to cellular regulation that together contribute to the complex pattern of loop heterogeneity observed in vivo. It is therefore imperative to build physical model representations of these features to be able to dissect the targets of cellular regulation.

Finally, *we propose that a major functionality of weak interactions in all eukaryotic cells is that it is the basis for the remarkable search algorithm that goes on constantly in cells.* How does a sequence-specific binding protein scan 3 billion base pairs that are folded around histone proteins and compacted into loops? How do gene-sized pieces of DNA (about 1000 base pairs) find homology when they need to be repaired following some environmental insult? In the vernacular of the day, the cell must employ its own well-honed, autonomous, "intelligent" mechanisms to make evolutionary, informed choices about how to find the relevant sequences or genomic regions for necessary tasks. The challenge on the current horizon is to more deeply understand the weak-interaction-induced power of soft cellular systems to simultaneously be open to self-exploration, especially in response to damage but also to changing environmental conditions, and yet hard-wired to execute cell-type specific functions.

The role of weak interactions in the functionality of respiratory mucus, indeed all mucus barriers throughout the human body, is only now coming into focus. An excellent recent "primer" on mucus is [130]. This article spans the chemical structure of the diverse mucin polymers that comprise the mucus barrier in tears, ears, the oral cavity, lungs, stomach, intestines, and the female cervicovaginal tract, and discusses the functionalities of each organ-specific mucus. The article likewise emphasizes the mysteries that remain in understanding how the ingredients of each mucus barrier induce its remarkable properties. What we have only recently come to realize [158] is that the functional properties of respiratory mucus are tuned by pervasive, weak interactions throughout the MUC5B and MUC5AC entangled polymer complex. And further as detailed in [135], in disease progression from individuals with cystic fibrosis (CF), significant modifications of the mucus hydrogel unfold. These modifications derive not only from an increase in the wt% of mucins due to poor hydration of the epithelial surface [158], but additionally due to changes in the ratio of MUC5AC to MUC5B as well as added by-products of chronic lung infection. These modifications of the mucus hydrogel lead to the dramatic changes noted in this review, in particular a progressive phase separation of the mucins into dense, insoluble raft-like structures called flakes. In the body of this review, we reported two separate current and unpublished results. The use of passive microbead experiments to probe synthetically reconstituted flake-prevalent mucus [139], and the use of molecular dynamics simulations coupled with experimental characterizations to illustrate that three chemical modifications of CF mucus cooperatively induce a phase separation of the polymeric mucins to form insoluble, dense flakes [135]. Similar pathologies are associated with abnormal mucus barriers on all organs, and the analogous molecular and chemical modifications are targets of intense study.

In our work on respiratory mucus, we foresee two potential outcomes on the near horizon made possible by the results presented in this review. First, we anticipate that the passive particle tracking "fractional Brownian motion classifier" can potentially provide a means to detect the current state of disease progression by performing passive particle tracking on clinical CF patient samples. Second, we anticipate that the discovery of the phase separation pathway to form mucus flakes, including the three chemical bases for the pathway, will point to chemical treatment strategies to reverse the phase separation process. Significant work lies ahead to realize these outcomes.

Declaration of competing interest

The authors declare the following financial interests/personal relationships which may be considered as potential competing interests: Kerry Bloom reports a relationship with National Institute of Health that includes: funding grants and non-financial support. Ronit Freeman reports a relationship with National Institutes of Health that includes: funding grants.

Data availability

Data will be made available on request.

Acknowledgement of financial support

For PAV: NSF-DMS 1751339 and the Rochester Institute of Technology and University of South Carolina Grant/Cooperative Agreement Number 80NSSC19K0159 P00004; for BW: NSF DMS-1816394 and the NSF-Simons Center for Multiscale Cell Fate Research; for ML: National Sciences and Engineering Research Council of Canada (NSERC) Discovery Grant RGPIN-2020-04364; for NC: NSF DMS-1929298; for CH: Gettysburg College faculty startup funds; for KN: NSF DMS-1816394 and DMS-2307297; for RF, MP, CE, and MGF: the Alfred P. Sloan Foundation award G-2021-14197; RF acknowledges financial support from Cottrell Scholar Award #CS-CSA-2023-033 sponsored by Research Corporation for Science Advancement, United States; for MGF: NSF DMS-1929298 and CISE-1931516.

References

[1] H. Flaschka, M.G. Forest, D.W. McLaughlin, Multiphase averaging and the inverse spectral solution of the kdv equation, Comm. Pure Appl. Math. 33 (1980) 739–784.

[2] N.M. Ercolani, M.G. Forest, The geometry of real sine-Gordon wavetrains, Comm. Math. Phys. 99 (1985) 1–49, http://dx.doi.org/10.1007/BF01466592.

[3] A.R. Bishop, D.W. McLaughlin, M.G. Forest, E.A. Overman, Quasi-periodic route to chaos in a near-integrable PDE: Homoclinic crossings, Phys. Lett. A 127 (1988) 335–340, http://dx.doi.org/10.1016/0375-9601(88)90580-4.

[4] A.R. Bishop, R. Flesch, M.G. Forest, D.W. McLaughlin, E.A. Overman II, Correlations between chaos in a perturbed Sine–Gordon equation and a truncated model system, SIAM J. Math. Anal. 21 (1990) 1511–1536, http://dx.doi.org/10.1137/0521083.

[5] Y. Li, D.W. McLaughlin, Morse and Melnikov functions for NLS PDEs, Comm. Math. Phys. 162 (1994) 175–214, http://dx.doi.org/10.1007/BF02105191.

[6] M.J. Ablowitz, B.M. Herbst, On homoclinic structure and numerically induced chaos for the nonlinear Schrödinger equation, SIAM J. Appl. Math. 50 (1990) 339–351, http://dx.doi.org/10.1137/0150021.

[7] G. Kovačič, S. Wiggins, Orbits homoclinic to resonances, with an application to chaos in a model of the forced and damped sine-Gordon equation, Physica D 57 (1992) 185–225, http://dx.doi.org/10.1016/0167-2789(92)90092-2.

[8] P.J. Oliver, A. Stern, Dispersive fractalisation in linear and nonlinear fermi–pasta–ulam–tsingou lattices, Eur. J. Appl. Math. 32 (5) (2021) 820–845.

[9] H. Flaschka, On the Toda lattice. II: Inverse-scattering solution, Progr. Theoret. Phys. 51 (1974) 703–716, http://dx.doi.org/10.1143/PTP.51.703.

[10] H. Flaschka, The Toda lattice. II. Existence of integrals, Phys. Rev. B 9 (1974) 1924–1925, http://dx.doi.org/10.1103/PhysRevB.9.1924.

[11] B.L. Holian, H. Flaschka, D.W. McLaughlin, Shock waves in the Toda lattice: Analysis, Phys. Rev. A 24 (1981) 2595–2623, http://dx.doi.org/10.1103/PhysRevA.24.2595.

[12] W.E. Ferguson, H. Flaschka, D.W. McLaughlin, Nonlinear normal modes for the Toda Chain, J. Comput. Phys. 45 (1982) 157–209, http://dx.doi.org/10.1016/0021-9991(82)90116-4.

[13] C. Ridley, D.J. Thornton, Mucins: the frontline defence of the lung, Biochem. Soc. Trans. 46 (2018) 1099–1106, http://dx.doi.org/10.1042/BST20170402.

[14] C.E. Wagner, K.M. Wheeler, K. Ribbeck, Mucins and their role in shaping the functions of mucus barriers, Annu. Rev. Cell Dev. Biol. 34 (2018) 189–215, http://dx.doi.org/10.1146/annurev-cellbio-100617-062818.

[15] T. Hirano, The ABCs of SMC proteins: two-armed ATPases for chromosome condensation, cohesion, and repair, Genes Dev. 16 (2002) 399–414, http://dx.doi.org/10.1101/gad.955102.

[16] A. Chen, S.A. McKinley, S. Wang, F. Shi, P.J. Mucha, M.G. Forest, S.K. Lai, Transient antibody-mucin interactions produce a dynamic molecular shield against viral invasion, Biophys. J. 106 (2014) 2028–2036, http://dx.doi.org/10.1016/j.bpj.2014.02.038.

[17] S.A. McKinley, A. Chen, F. Shi, S. Wang, P.J. Mucha, M.G. Forest, S.K. Lai, Modeling neutralization kinetics of HIV by broadly neutralizing monoclonal antibodies in genital secretions coating the cervicovaginal mucosa, PLoS ONE 9 (2014) e100598, http://dx.doi.org/10.1371/journal.pone.0100598.

[18] A. Chen, S.A. McKinley, F. Shi, S. Wang, P.J. Mucha, D. Harit, M.G. Forest, S.K. Lai, Modeling of virion collisions in cervicovaginal mucus reveals limits on agglutination as the protective mechanism of secretory immunoglobulin A, PLoS ONE 10 (2015) e0131351, http://dx.doi.org/10.1371/journal.pone.0131351.

[19] T. Wessler, A. Chen, S.A. McKinley, R. Cone, M.G. Forest, S.K. Lai, Using computational modeling to optimize the design of antibodies that trap viruses in mucus, ACS Infect. Dis. 2 (2016) 82–92, http://dx.doi.org/10.1021/acsinfecdis.5b00108.

[20] J. Newby, J.L. Schiller, T. Wessler, J. Edelstein, M.G. Forest, S.K. Lai, A blueprint for robust crosslinking of mobile species in biogels with weakly adhesive molecular anchors, Nature Commun. 8 (2017) 833, http://dx.doi.org/10.1038/s41467-017-00739-6.

[21] M.A. Jensen, Y.-Y. Wang, S.K. Lai, M.G. Forest, S.A. McKinley, Antibody-mediated immobilization of virions in mucus, Bull. Math. Biol. 81 (2019) 4069–4099, http://dx.doi.org/10.1007/s11538-019-00653-6.

[22] F. Xu, J.M. Newby, J.L. Schiller, H.A. Schroeder, T. Wessler, A. Chen, M.G. Forest, S.K. Lai, Modeling barrier properties of intestinal mucus reinforced with IgG and secretory IgA against motile bacteria, ACS Infect. Dis. 5 (2019) 1570–1580, http://dx.doi.org/10.1021/acsinfecdis.9b00109.

[23] H.A. Schroeder, J. Newby, A. Schaefer, B. Subramani, A. Tubbs, M. Gregory Forest, E. Miao, S.K. Lai, LPS-binding IgG arrests actively motile Salmonella Typhimurium in gastrointestinal mucus, Mucosal Immunol. 13 (2020) 814–823, http://dx.doi.org/10.1038/s41385-020-0267-9.

[24] A. Chen, T. Wessler, K. Daftari, K. Hinton, R.C. Boucher, R. Pickles, R. Freeman, S.K. Lai, M.G. Forest, Modeling insights into SARS-CoV-2 respiratory tract infections prior to immune protection, Biophys. J. 121 (2022) 1619–1631, http://dx.doi.org/10.1016/j.bpj.2022.04.003.

[25] C. Darquenne, A.A.T. Borojeni, M.J. Colebank, M.G. Forest, B.G. Madas, M. Tawhai, Y. Jiang, Aerosol transport modeling: The key link between lung infections of individuals and populations, Front. Physiol. 13 (2022) 923945, http://dx.doi.org/10.3389/fphys.2022.923945.

[26] A.C. Aristotelous, A. Chen, M.G. Forest, A hybrid discrete-continuum model of immune responses to SARS-CoV-2 infection in the lung alveolar region, with a focus on interferon induced innate response, J. Theoret. Biol. 555 (2022) 111293, http://dx.doi.org/10.1016/j.jtbi.2022.111293.

[27] A. Chen, T. Wessler, M. Gregory Forest, Antibody protection from SARS-CoV-2 respiratory tract exposure and infection, J. Theoret. Biol. 557 (2023) 111334, http://dx.doi.org/10.1016/j.jtbi.2022.111334.

[28] N.V. Dokholyan (Ed.), Computational Modeling of Biological Systems: From Molecules to Pathways, Springer, New York Heidelberg, 2012.

[29] M. Kapustina, D. Tsygankov, J. Zhao, T. Wessler, X. Yang, A. Chen, N. Roach, T.C. Elston, Q. Wang, K. Jacobson, M.G. Forest, Modeling the excess cell surface stored in a complex morphology of bleb-like protrusions, PLoS Comput. Biol. 12 (2016) e1004841, http://dx.doi.org/10.1371/journal.pcbi.1004841.

[30] K. Gasior, J. Zhao, G. McLaughlin, M.G. Forest, A.S. Gladfelter, J. Newby, Partial demixing of RNA-protein complexes leads to intradroplet patterning in phase-separated biological condensates, Phys. Rev. E 99 (2019) 012411, http://dx.doi.org/10.1103/PhysRevE.99.012411.

[31] G.A. McLaughlin, E.M. Langdon, J.M. Crutchley, L.J. Holt, M.G. Forest, J.M. Newby, A.S. Gladfelter, Spatial heterogeneity of the cytosol revealed by machine learning-based 3D particle tracking, MBoC 31 (2020) 1498–1511, http://dx.doi.org/10.1091/mbc.E20-03-0210.

[32] K. Gasior, M.G. Forest, A.S. Gladfelter, J.M. Newby, Modeling the mechanisms by which coexisting biomolecular RNA–protein condensates form, Bull. Math. Biol. 82 (2020) 153, http://dx.doi.org/10.1007/s11538-020-00823-x.

[33] K.B. Patel, S. Mao, M.G. Forest, S.K. Lai, J.M. Newby, Limited processivity of single motors improves overall transport flux of self-assembled motor-cargo complexes, Phys. Rev. E 100 (2019) 022408, http://dx.doi.org/10.1103/PhysRevE.100.022408.

[34] L. Miao, J.M. Newby, C.M. Lin, L. Zhang, F. Xu, W.Y. Kim, M.G. Forest, S.K. Lai, M.I. Milowsky, S.E. Wobker, L. Huang, The binding site barrier elicited by tumor-associated fibroblasts interferes disposition of nanoparticles in stroma-vessel type tumors, ACS Nano 10 (2016) 9243–9258, http://dx.doi.org/10.1021/acsnano.6b02776.

[35] J.M. Newby, I. Seim, M. Lysy, Y. Ling, J. Huckaby, S.K. Lai, M.G. Forest, Technological strategies to estimate and control diffusive passage times through the mucus barrier in mucosal drug delivery, Adv. Drug Deliv. Rev. 124 (2018) 64–81, http://dx.doi.org/10.1016/j.addr.2017.12.002.

[36] M.D. McSweeney, T. Wessler, L.S.L. Price, E.C. Ciociola, L.B. Herity, J.A. Piscitelli, W.C. Zamboni, M.G. Forest, Y. Cao, S.K. Lai, A minimal physiologically based pharmacokinetic model that predicts anti-PEG IgG-mediated clearance of PEGylated drugs in human and mouse, J. Control. Release 284 (2018) 171–178, http://dx.doi.org/10.1016/j.jconrel.2018.06.002.

[37] M.D. McSweeney, L.S.L. Price, T. Wessler, E.C. Ciociola, L.B. Herity, J.A. Piscitelli, A.C. DeWalle, T.N. Harris, A.K.P. Chan, R.S. Saw, P. Hu, J.C. Jennette, M.G. Forest, Y. Cao, S.A. Montgomery, W.C. Zamboni, S.K. Lai, Overcoming anti-PEG antibody mediated accelerated blood clearance of PEGylated liposomes by pre-infusion with high molecular weight free PEG, J. Control. Release 311–312 (2019) 138–146, http://dx.doi.org/10.1016/j.jconrel.2019.08.017.

[38] A.M. Talkington, T. Wessler, S.K. Lai, Y. Cao, M.G. Forest, Experimental data and PBPK modeling quantify antibody interference in PEGylated drug carrier delivery, Bull. Math. Biol. 83 (2021) 123, http://dx.doi.org/10.1007/s11538-021-00950-z.

[39] A.M. Talkington, M.D. McSweeney, T. Wessler, M.K. Rath, Z. Li, T. Zhang, H. Yuan, J.E. Frank, M.G. Forest, Y. Cao, S.K. Lai, A PBPK model recapitulates early kinetics of anti-PEG antibody-mediated clearance of PEG-liposomes, J. Control. Release 343 (2022) 518–527, http://dx.doi.org/10.1016/j.jconrel.2022.01.022.

[40] A. Goffeau, B.G. Barrell, H. Bussey, R.W. Davis, B. Dujon, H. Feldmann, F. Galibert, J.D. Hoheisel, C. Jacq, M. Johnston, E.J. Louis, H.W. Mewes, Y. Murakami, P. Philippsen, H. Tettelin, S.G. Oliver, Life with 6000 genes, Science 274 (1996) 546–567, http://dx.doi.org/10.1126/science.274.5287.546.

[41] S. Nurk, S. Koren, A. Rhie, M. Rautiainen, A.V. Bzikadze, A. Mikheenko, M.R. Vollger, N. Altemose, L. Uralsky, A. Gershman, S. Aganezov, S.J. Hoyt, M. Diekhans, G.A. Logsdon, M. Alonge, S.E. Antonarakis, M. Borchers, G.G. Bouffard, S.Y. Brooks, G.V. Caldas, N.-C. Chen, H. Cheng, C.-S. Chin, W. Chow, L.G. de Lima, P.C. Dishuck, R. Durbin, T. Dvorkina, I.T. Fiddes, G. Formenti, R.S. Fulton, A. Fungtammasan, E. Garrison, P.G.S. Grady, T.A. Graves-Lindsay, I.M. Hall, N.F. Hansen, G.A. Hartley, M. Haukness, K. Howe, M.W. Hunkapiller, C. Jain, M. Jain, E.D. Jarvis, P. Kerpedjiev, M. Kirsche, M. Kolmogorov, J. Korlach, M. Kremitzki, H. Li, V.V. Maduro, T. Marschall, A.M. McCartney, J. McDaniel, D.E. Miller, J.C. Mullikin, E.W. Myers, N.D. Olson, B. Paten, P. Peluso, P.A. Pevzner, D. Porubsky, T. Potapova, E.I. Rogaev, J.A. Rosenfeld, S.L. Salzberg, V.A. Schneider, F.J. Sedlazeck, K. Shafin, C.J. Shew, A. Shumate, Y. Sims, A.F.A. Smit, D.C. Soto, I. Sović, J.M. Storer, A. Streets, B.A. Sullivan, F. Thibaud-Nissen, J. Torrance, J. Wagner, B.P. Walenz, A. Wenger, J.M.D. Wood, C. Xiao, S.M. Yan, A.C.

Young, S. Zarate, U. Surti, R.C. McCoy, M.Y. Dennis, I.A. Alexandrov, J.L. Gerton, R.J. O'Neill, W. Timp, J.M. Zook, M.C. Schatz, E.E. Eichler, K.H. Miga, A.M. Phillippy, The complete sequence of a human genome, Science 376 (2022) 44–53, http://dx.doi.org/10.1126/science.abj6987.
[42] S.G. Oliver, Functional genomics: lessons from yeast, Phil. Trans. R. Soc. Lond. B 357 (2002) 17–23, http://dx.doi.org/10.1098/rstb.2001.1049.
[43] A. Hamza, E. Tammpere, M. Kofoed, C. Keong, J. Chiang, G. Giaever, C. Nislow, P. Hieter, Complementation of yeast genes with human genes as an experimental platform for functional testing of human genetic variants, Genetics 201 (2015) 1263–1274, http://dx.doi.org/10.1534/genetics.115.181099.
[44] P.C. Stirling, M.S. Bloom, T. Solanki-Patil, S. Smith, P. Sipahimalani, Z. Li, M. Kofoed, S. Ben-Aroya, K. Myung, P. Hieter, The complete spectrum of yeast chromosome instability genes identifies candidate CIN cancer genes and functional roles for ASTRA complex components, PLoS Genet. 7 (2011) e1002057, http://dx.doi.org/10.1371/journal.pgen.1002057.
[45] F. Perocchi, E. Mancera, L.M. Steinmetz, Systematic screens for human disease genes, from yeast to human and back, Mol. BioSyst. 4 (2008) 18–29, http://dx.doi.org/10.1039/B709494A.
[46] P. Gaspar, I. Almudi, M.D.S. Nunes, A.P. McGregor, Human eye conditions: insights from the fly eye, Hum. Genet. 138 (2019) 973–991, http://dx.doi.org/10.1007/s00439-018-1948-2.
[47] E. Lieberman-Aiden, N.L. van Berkum, L. Williams, M. Imakaev, T. Ragoczy, A. Telling, I. Amit, B.R. Lajoie, P.J. Sabo, M.O. Dorschner, R. Sandstrom, B. Bernstein, M.A. Bender, M. Groudine, A. Gnirke, J. Stamatoyannopoulos, L.A. Mirny, E.S. Lander, J. Dekker, Comprehensive mapping of long-range interactions reveals folding principles of the human genome, Science 326 (2009) 289–293, http://dx.doi.org/10.1126/science.1181369.
[48] J. Dekker, The three C s of chromosome conformation capture: controls, controls, controls, Nature Methods 3 (2006) 17–21, http://dx.doi.org/10.1038/nmeth823.
[49] B. Walker, D. Taylor, J. Lawrimore, C. Hult, D. Adalsteinsson, K. Bloom, M.G. Forest, Transient crosslinking kinetics optimize gene cluster interactions, PLoS Comput. Biol. 15 (2019) e1007124, http://dx.doi.org/10.1371/journal.pcbi.1007124.
[50] C. Hult, D. Adalsteinsson, P.A. Vasquez, J. Lawrimore, M. Bennett, A. York, D. Cook, E. Yeh, M.G. Forest, K. Bloom, Enrichment of dynamic chromosomal crosslinks drive phase separation of the nucleolus, Nucleic Acids Res. 45 (2017) 11159–11173, http://dx.doi.org/10.1093/nar/gkx741.
[51] G. Felsenfeld, M. Groudine, Controlling the double helix, Nature 421 (2003) 448–453, http://dx.doi.org/10.1038/nature01411.
[52] J. Mateos-Langerak, M. Bohn, W. de Leeuw, O. Giromus, E.M.M. Manders, P.J. Verschure, M.H.G. Indemans, H.J. Gierman, D.W. Heermann, R. van Driel, S. Goetze, Spatially confined folding of chromatin in the interphase nucleus, Proc. Natl. Acad. Sci. USA 106 (2009) 3812–3817, http://dx.doi.org/10.1073/pnas.0809501106.
[53] P.A. Vasquez, K. Bloom, Polymer models of interphase chromosomes, Nucleus 5 (2014) 376–390, http://dx.doi.org/10.4161/nucl.36275.
[54] J.S. Verdaasdonk, P.A. Vasquez, R.M. Barry, T. Barry, S. Goodwin, M.G. Forest, K. Bloom, Centromere tethering confines chromosome domains, Mol. Cell 52 (2013) 819–831, http://dx.doi.org/10.1016/j.molcel.2013.10.021.
[55] R. Wang, J. Mozziconacci, A. Bancaud, O. Gadal, Principles of chromatin organization in yeast: relevance of polymer models to describe nuclear organization and dynamics, Curr. Opin. Cell Biol. 34 (2015) 54–60, http://dx.doi.org/10.1016/j.ceb.2015.04.004.
[56] H. Tjong, K. Gong, L. Chen, F. Alber, Physical tethering and volume exclusion determine higher-order genome organization in budding yeast, Genome Res. 22 (2012) 1295–1305, http://dx.doi.org/10.1101/gr.129437.111.
[57] T. Misteli, E. Soutoglou, The emerging role of nuclear architecture in DNA repair and genome maintenance, Nat. Rev. Mol. Cell Biol. 10 (2009) 243–254, http://dx.doi.org/10.1038/nrm2651.
[58] A. Taddei, H. Schober, S.M. Gasser, The budding yeast nucleus, Cold Spring Harb. Perspect. Biol. 2 (2010) a000612, http://dx.doi.org/10.1101/cshperspect.a000612.
[59] T. Takizawa, K.J. Meaburn, T. Misteli, The meaning of gene positioning, Cell 135 (2008) 9–13, http://dx.doi.org/10.1016/j.cell.2008.09.026.
[60] S.T. Spagnol, T.J. Armiger, K.N. Dahl, Mechanobiology of chromatin and the nuclear interior, Cell. Mol. Bioeng. 9 (2016) 268–276, http://dx.doi.org/10.1007/s12195-016-0444-9.
[61] C.W. Quammen, A.C. Richardson, J. Haase, B.D. Harrison, R.M.T. II, K.S. Bloom, FluoroSim: A visual problem-solving environment for fluorescence microscopy, in: Eurographics Workshop on Visual Computing for Biomedicine, 2008, p. 8, http://dx.doi.org/10.2312/VCBM/VCBM08/151-158.
[62] A.D. Stephens, R.A. Haggerty, P.A. Vasquez, L. Vicci, C.E. Snider, F. Shi, C. Quammen, C. Mullins, J. Haase, R.M. Taylor, J.S. Verdaasdonk, M.R. Falvo, Y. Jin, M.G. Forest, K. Bloom, Pericentric chromatin loops function as a nonlinear spring in mitotic force balance, J. Cell Biol. 200 (2013) 757–772, http://dx.doi.org/10.1083/jcb.201208163.
[63] A.D. Stephens, C.E. Snider, J. Haase, R.A. Haggerty, P.A. Vasquez, M.G. Forest, K. Bloom, Individual pericentromeres display coordinated motion and stretching in the yeast spindle, J. Cell Biol. 203 (2013) 407–416, http://dx.doi.org/10.1083/jcb.201307104.
[64] J. Lawrimore, P.A. Vasquez, M.R. Falvo, R.M. Taylor, L. Vicci, E. Yeh, M.G. Forest, K. Bloom, DNA loops generate intracentromere tension in mitosis, J. Cell Biol. 210 (2015) 553–564, http://dx.doi.org/10.1083/jcb.201502046.
[65] P.A. Vasquez, C. Hult, D. Adalsteinsson, J. Lawrimore, M.G. Forest, K. Bloom, Entropy gives rise to topologically associating domains, Nucleic Acids Res. 44 (2016) 5540–5549, http://dx.doi.org/10.1093/nar/gkw510.
[66] M. Hochstrasser, D. Mathog, Y. Gruenbaum, H. Saumweber, J.W. Sedat, Spatial organization of chromosomes in the salivary gland nuclei of Drosophila melanogaster, J. Cell Biol. 102 (1986) 112–123, http://dx.doi.org/10.1083/jcb.102.1.112.
[67] H. Wong, J.-M. Arbona, C. Zimmer, How to build a yeast nucleus, Nucleus 4 (2013) 361–366, http://dx.doi.org/10.4161/nucl.26226.
[68] H. Wong, H. Marie-Nelly, S. Herbert, P. Carrivain, H. Blanc, R. Koszul, E. Fabre, C. Zimmer, A predictive computational model of the dynamic 3D interphase yeast nucleus, Curr. Biol. 22 (2012) 1881–1890, http://dx.doi.org/10.1016/j.cub.2012.07.069.
[69] the 4D Nucleome Network, J. Dekker, A.S. Belmont, M. Guttman, V.O. Leshyk, J.T. Lis, S. Lomvardas, L.A. Mirny, C.C. O'Shea, P.J. Park, B. Ren, J.C.R. Politz, J. Shendure, S. Zhong, The 4D nucleome project, Nature 549 (2017) 219–226, http://dx.doi.org/10.1038/nature23884.
[70] J. Dekker, F. Alber, S. Aufmkolk, B.J. Beliveau, B.G. Bruneau, A.S. Belmont, L. Bintu, A. Boettiger, R. Calandrelli, C.M. Disteche, D.M. Gilbert, T. Gregor, A.S. Hansen, B. Huang, D. Huangfu, R. Kalhor, C.S. Leslie, W. Li, Y. Li, J. Ma, W.S. Noble, P.J. Park, J.E. Phillips-Cremins, K.S. Pollard, S.M. Rafelski, B. Ren, Y. Ruan, Y. Shav-Tal, Y. Shen, J. Shendure, X. Shu, C. Strambio-De-Castillia, A. Vertii, H. Zhang, S. Zhong, Spatial and temporal organization of the genome: Current state and future aims of the 4D nucleome project, Mol. Cell (2023) S1097276523004653, http://dx.doi.org/10.1016/j.molcel.2023.06.018.
[71] C. Zimmer, E. Fabre, Principles of chromosomal organization: lessons from yeast, J. Cell Biol. 192 (2011) 723–733, http://dx.doi.org/10.1083/jcb.201010058.
[72] M.H. Hauer, S.M. Gasser, Chromatin and nucleosome dynamics in DNA damage and repair, Genes Dev. 31 (2017) 2204–2221, http://dx.doi.org/10.1101/gad.307702.117.
[73] J. Lawrimore, K. Bloom, The regulation of chromosome segregation via centromere loops, Crit. Rev. Biochem. Mol. Biol. 54 (2019) 352–370, http://dx.doi.org/10.1080/10409238.2019.1670130.
[74] J. Lawrimore, T.M. Barry, R.M. Barry, A.C. York, B. Friedman, D.M. Cook, K. Akialis, J. Tyler, P. Vasquez, E. Yeh, K. Bloom, Microtubule dynamics drive enhanced chromatin motion and mobilize telomeres in response to DNA damage, MBoC 28 (2017) 1701–1711, http://dx.doi.org/10.1091/mbc.e16-12-0846.
[75] M. Socol, R. Wang, D. Jost, P. Carrivain, C. Vaillant, E. Le Cam, V. Dahirel, C. Normand, K. Bystricky, J.-M. Victor, O. Gadal, A. Bancaud, Rouse model with transient intramolecular contacts on a timescale of seconds recapitulates folding and fluctuation of yeast chromosomes, Nucleic Acids Res. 47 (2019) 6195–6207, http://dx.doi.org/10.1093/nar/gkz374.
[76] I.M. Flyamer, J. Gassler, M. Imakaev, H.B. Brandão, S.V. Ulianov, N. Abdennur, S.V. Razin, L.A. Mirny, K. Tachibana-Konwalski, Single-nucleus Hi-C reveals unique chromatin reorganization at oocyte-to-zygote transition, Nature 544 (2017) 110–114, http://dx.doi.org/10.1038/nature21711.
[77] C. Dai, W. Li, H. Tjong, S. Hao, Y. Zhou, Q. Li, L. Chen, B. Zhu, F. Alber, X. Jasmine Zhou, Mining 3D genome structure populations identifies major factors governing the stability of regulatory communities, Nature Commun. 7 (2016) 11549, http://dx.doi.org/10.1038/ncomms11549.
[78] G. Fudenberg, M. Imakaev, C. Lu, A. Goloborodko, N. Abdennur, L.A. Mirny, Formation of chromosomal domains by loop extrusion, Cell Rep. 15 (2016) 2038–2049, http://dx.doi.org/10.1016/j.celrep.2016.04.085.
[79] R.G. Larson, The rheology of dilute solutions of flexible polymers: Progress and problems, J. Rheol. 49 (2005) 1–70, http://dx.doi.org/10.1122/1.1835336.
[80] P.T. Underhill, P.S. Doyle, Accuracy of bead–spring chains in strong flows, J. Non-Newton. Fluid Mech. 145 (2007) 109–123, http://dx.doi.org/10.1016/j.jnnfm.2007.05.011.
[81] D. Saintillan, M.J. Shelley, A. Zidovska, Extensile motor activity drives coherent motions in a model of interphase chromatin, Proc. Natl. Acad. Sci. USA 115 (2018) 11442–11447, http://dx.doi.org/10.1073/pnas.1807073115.
[82] A. Zidovska, The self-stirred genome: large-scale chromatin dynamics, its biophysical origins and implications, Curr. Opin. Genet. Dev. 61 (2020) 83–90, http://dx.doi.org/10.1016/j.gde.2020.03.008.
[83] A. Mahajan, W. Yan, A. Zidovska, D. Saintillan, M.J. Shelley, Euchromatin activity enhances segregation and compaction of heterochromatin in the cell nucleus, Phys. Rev. X 12 (2022) 041033, http://dx.doi.org/10.1103/PhysRevX.12.041033.

[84] J.F. Marko, E.D. Siggia, Bending and twisting elasticity of DNA, Macromolecules 27 (1994) 981–988, http://dx.doi.org/10.1021/ma00082a015.
[85] J.F. Marko, E.D. Siggia, Stretching DNA, Macromolecules 28 (1995) 8759–8770, http://dx.doi.org/10.1021/ma00130a008.
[86] J.K. Fisher, M. Ballenger, E.T. O'Brien, J. Haase, R. Superfine, K. Bloom, DNA relaxation dynamics as a probe for the intracellular environment, Proc. Natl. Acad. Sci. USA 106 (2009) 9250–9255, http://dx.doi.org/10.1073/pnas.0812723106.
[87] R.M. Jendrejack, J.J. de Pablo, M.D. Graham, Stochastic simulations of DNA in flow: Dynamics and the effects of hydrodynamic interactions, J. Chem. Phys. 116 (2002) 7752–7759, http://dx.doi.org/10.1063/1.1466831.
[88] D.M. Heyes, J.R. Melrose, Brownian dynamics simulations of model hard-sphere suspensions, J. Non-Newton. Fluid Mech. 46 (1993) 1–28, http://dx.doi.org/10.1016/0377-0257(93)80001-R.
[89] T. Cremer, C. Cremer, Chromosome territories, nuclear architecture and gene regulation in mammalian cells, Nat. Rev. Genet. 2 (2001) 292–301, http://dx.doi.org/10.1038/35066075.
[90] J.R. Dixon, S. Selvaraj, F. Yue, A. Kim, Y. Li, Y. Shen, M. Hu, J.S. Liu, B. Ren, Topological domains in mammalian genomes identified by analysis of chromatin interactions, Nature 485 (2012) 376–380, http://dx.doi.org/10.1038/nature11082.
[91] V. Dion, V. Kalck, C. Horigome, B.D. Towbin, S.M. Gasser, Increased mobility of double-strand breaks requires Mec1, Rad9 and the homologous recombination machinery, Nat. Cell Biol. 14 (2012) 502–509, http://dx.doi.org/10.1038/ncb2465.
[92] A. Seeber, V. Dion, S.M. Gasser, Checkpoint kinases and the INO80 nucleosome remodeling complex enhance global chromatin mobility in response to DNA damage, Genes Dev. 27 (2013) 1999–2008, http://dx.doi.org/10.1101/gad.222992.113.
[93] M.H. Hauer, A. Seeber, V. Singh, R. Thierry, R. Sack, A. Amitai, M. Kryzhanovska, J. Eglinger, D. Holcman, T. Owen-Hughes, S.M. Gasser, Histone degradation in response to DNA damage enhances chromatin dynamics and recombination rates, Nat. Struct. Mol. Biol. 24 (2017) 99–107, http://dx.doi.org/10.1038/nsmb.3347.
[94] J. Miné-Hattab, R. Rothstein, Increased chromosome mobility facilitates homology search during recombination, Nat. Cell Biol. 14 (2012) 510–517, http://dx.doi.org/10.1038/ncb2472.
[95] V. Roukos, T.C. Voss, C.K. Schmidt, S. Lee, D. Wangsa, T. Misteli, Spatial dynamics of chromosome translocations in living cells, Science 341 (2013) 660–664, http://dx.doi.org/10.1126/science.1237150.
[96] J. Strecker, G.D. Gupta, W. Zhang, M. Bashkurov, M.-C. Landry, L. Pelletier, D. Durocher, DNA damage signalling targets the kinetochore to promote chromatin mobility, Nat. Cell Biol. 18 (2016) 281–290, http://dx.doi.org/10.1038/ncb3308.
[97] C. Michaelis, R. Ciosk, K. Nasmyth, Cohesins: Chromosomal proteins that prevent premature separation of sister chromatids, Cell 91 (1997) 35–45, http://dx.doi.org/10.1016/S0092-8674(01)80007-6.
[98] A.D. Stephens, J. Haase, L. Vicci, R.M. Taylor, K. Bloom, Cohesin, condensin, and the intramolecular centromere loop together generate the mitotic chromatin spring, J. Cell Biol. 193 (2011) 1167–1180, http://dx.doi.org/10.1083/jcb.201103138.
[99] W. Weir, S. Emmons, R. Gibson, D. Taylor, P. Mucha, Post-processing partitions to identify domains of modularity optimization, Algorithms 10 (2017) 93, http://dx.doi.org/10.3390/a10030093.
[100] B.L. Walker, K.A. Newhall, Numerical computation of effective thermal equilibria in stochastically switching Langevin systems, Phys. Rev. E 105 (2022) 064113, http://dx.doi.org/10.1103/PhysRevE.105.064113.
[101] A. Allen, G. Flemstrom, A. Garner, E. Kivilaakso, Gastroduodenal mucosal protection, Physiol. Rev. 73 (1993) 823–857, http://dx.doi.org/10.1152/physrev.1993.73.4.823.
[102] A. Silberberg, Rheology of mucus, mucociliary interaction, and ciliary activity, Cell Motil. 2 (1982) 25–28, http://dx.doi.org/10.1002/cm.970020707.
[103] D.F. Katz, Human cervical mucus: Research update, Am. J. Obstet. Gynecol. 165 (1991) 1984–1986, http://dx.doi.org/10.1016/S0002-9378(11)90559-6.
[104] R.A. Cone, Barrier properties of mucus, Adv. Drug Deliv. Rev. 61 (2009) 75–85, http://dx.doi.org/10.1016/j.addr.2008.09.008.
[105] M.R. Knowles, R.C. Boucher, Mucus clearance as a primary innate defense mechanism for mammalian airways, J. Clin. Invest. 109 (2002) 571–577, http://dx.doi.org/10.1172/JCI0215217.
[106] S.K. Lai, Y.-Y. Wang, D. Wirtz, J. Hanes, Micro- and macrorheology of mucus, Adv. Drug Deliv. Rev. 61 (2009) 86–100, http://dx.doi.org/10.1016/j.addr.2008.09.012.
[107] D.J. Thornton, J.K. Sheehan, From mucins to mucus, Proc. Am. Thorac. Soc. 1 (2004) 54–61, http://dx.doi.org/10.1513/pats.2306016.
[108] L.A. Sellers, A. Allen, E.R. Morris, S.B. Ross-Murphy, Mucus glycoprotein gels. Role of glycoprotein polymeric structure and carbohydrate side-chains in gel-formation, Carbohydr. Res. 178 (1988) 93–110, http://dx.doi.org/10.1016/0008-6215(88)80104-6.
[109] C. Taylor, A. Allen, P.W. Dettmar, J.P. Pearson, The gel matrix of gastric mucus is maintained by a complex interplay of transient and nontransient associations, Biomacromolecules 4 (2003) 922–927, http://dx.doi.org/10.1021/bm025767t.
[110] P. Verdugo, Supramolecular dynamics of mucus, Cold Spring Harb. Perspect. Med. 2 (2012) a009597, http://dx.doi.org/10.1101/cshperspect.a009597.
[111] X. Cao, R. Bansil, K.R. Bhaskar, B.S. Turner, J.T. LaMont, N. Niu, N.H. Afdhal, pH-dependent conformational change of gastric mucin leads to sol-gel transition, Biophys. J. 76 (1999) 1250–1258, http://dx.doi.org/10.1016/S0006-3495(99)77288-7.
[112] J.P. Celli, B.S. Turner, N.H. Afdhal, R.H. Ewoldt, G.H. McKinley, R. Bansil, S. Erramilli, Rheology of gastric mucin exhibits a pH-dependent sol-gel transition, Biomacromolecules 8 (2007) 1580–1586, http://dx.doi.org/10.1021/bm0609691.
[113] P. Gniewek, A. Kolinski, Coarse-grained Monte Carlo simulations of mucus: Structure, dynamics, and thermodynamics, Biophys. J. 99 (2010) 3507–3516, http://dx.doi.org/10.1016/j.bpj.2010.09.047.
[114] J.K. Sheehan, C. Hanski, A.P. Corfield, C. Paraskeva, D.J. Thornton, Mucin biosynthesis and macromolecular assembly, Biochem. Soc. Trans. 23 (1995) 819–821, http://dx.doi.org/10.1042/bst0230819.
[115] G.E. Yakubov, A. Papagiannopoulos, E. Rat, T.A. Waigh, Charge and interfacial behavior of short side-chain heavily glycosylated porcine stomach mucin, Biomacromolecules 8 (2007) 3791–3799, http://dx.doi.org/10.1021/bm700721c.
[116] J. Dekker, J.W.A. Rossen, H.A. Büller, A.W.C. Einerhand, The MUC family: an obituary, Trends Biochem. Sci. 27 (2002) 126–131, http://dx.doi.org/10.1016/S0968-0004(01)02052-7.
[117] J. Pearson, T. Wessler, A. Chen, R.C. Boucher, R. Freeman, S.K. Lai, R. Pickles, M.G. Forest, Modeling identifies variability in SARS-CoV-2 uptake and eclipse phase by infected cells as principal drivers of extreme variability in nasal viral load in the 48 h post infection, J. Theoret. Biol. 565 (2023) 111470, http://dx.doi.org/10.1016/j.jtbi.2023.111470.
[118] D.B. Hill, P.A. Vasquez, J. Mellnik, S.A. McKinley, A. Vose, F. Mu, A.G. Henderson, S.H. Donaldson, N.E. Alexis, R.C. Boucher, M.G. Forest, A biophysical basis for mucus solids concentration as a candidate biomarker for airways disease, PLoS ONE 9 (2014) e87681, http://dx.doi.org/10.1371/journal.pone.0087681.
[119] P.A. Vasquez, M.G. Forest, Complex fluids and soft structures in the human body, in: S.E. Spagnolie (Ed.), Complex Fluids in Biological Systems, Springer New York, New York, NY, 2015, pp. 53–110, http://dx.doi.org/10.1007/978-1-4939-2065-5_2.
[120] C. Taylor, Two rheologically different gastric mucus secretions with different putative functions, Biochim. Biophys. Acta (BBA) - Gen. Subj. (2004) http://dx.doi.org/10.1016/j.bbagen.2004.06.007.
[121] S. Girod, J. Zahm, C. Plotkowski, G. Beck, E. Puchelle, Role of the physiochemical properties of mucus in the protection of the respiratory epithelium, Eur. Respir. J. 5 (1992) 477–487, http://dx.doi.org/10.1183/09031936.93.05040477.
[122] S.M. Gouveia, J.M. Tiffany, Human tear viscosity: An interactive role for proteins and lipids, Biochim. Biophys. Acta (BBA) - Proteins Proteom. 1753 (2005) 155–163, http://dx.doi.org/10.1016/j.bbapap.2005.08.023.
[123] A.E. Bell, L.A. Sellers, A. Allen, W.J. Cunliffe, E.R. Morris, S.B. Ross-Murphy, Properties of gastric and duodenal mucus: Effect of proteolysis, disulfide reduction, bile, acid, ethanol, and hypertonicity on mucus gel structure, Gastroenterology 88 (1985) 269–280, http://dx.doi.org/10.1016/S0016-5085(85)80180-3.
[124] K.R. Bhaskar, D.H. Gong, R. Bansil, S. Pajevic, J.A. Hamilton, B.S. Turner, J.T. LaMont, Profound increase in viscosity and aggregation of pig gastric mucin at low pH, Am. J. Physiol.-Gastrointest. Liver Physiol. 261 (1991) G827–G832, http://dx.doi.org/10.1152/ajpgi.1991.261.5.G827.
[125] C.E. Wagner, B.S. Turner, M. Rubinstein, G.H. McKinley, K. Ribbeck, A rheological study of the association and dynamics of MUC5AC gels, Biomacromolecules 18 (2017) 3654–3664, http://dx.doi.org/10.1021/acs.biomac.7b00809.
[126] D.B. Hill, R.F. Long, W.J. Kissner, E. Atieh, I.C. Garbarine, M.R. Markovetz, N.C. Fontana, M. Christy, M. Habibpour, R. Tarran, M.G. Forest, R.C. Boucher, B. Button, Pathological mucus and impaired mucus clearance in cystic fibrosis patients result from increased concentration, not altered pH, Eur. Respir. J. 52 (2018) 1801297, http://dx.doi.org/10.1183/13993003.01297-2018.
[127] M. Jory, K. Bellouma, C. Blanc, L. Casanellas, A. Petit, P. Reynaud, C. Vernisse, I. Vachier, A. Bourdin, G. Massiera, Mucus microrheology measured on human bronchial epithelium culture, Front. Phys. 7 (2019) 19, http://dx.doi.org/10.3389/fphy.2019.00019.
[128] M. Jory, D. Donnarumma, C. Blanc, K. Bellouma, A. Fort, I. Vachier, L. Casanellas, A. Bourdin, G. Massiera, Mucus from human bronchial epithelial cultures: rheology and adhesion across length scales, Interface Focus 12 (2022) 20220028, http://dx.doi.org/10.1098/rsfs.2022.0028.

[129] K.R. Rouillard, W.J. Kissner, M.R. Markovetz, D.B. Hill, Effects of mucin and DNA concentrations in airway mucus on pseudomonas aeruginosa biofilm recalcitrance, MSphere 7 (2022) e00291–22, http://dx.doi.org/10.1128/msphere.00291-22.
[130] A. McShane, J. Bath, A.M. Jaramillo, C. Ridley, A.A. Walsh, C.M. Evans, D.J. Thornton, K. Ribbeck, Mucus, Curr. Biol. 31 (2021) R938–R945, http://dx.doi.org/10.1016/j.cub.2021.06.093.
[131] R. Bansil, B.S. Turner, The biology of mucus: Composition, synthesis and organization, Adv. Drug Deliv. Rev. 124 (2018) 3–15, http://dx.doi.org/10.1016/j.addr.2017.09.023.
[132] J. Kirch, A. Schneider, B. Abou, A. Hopf, U.F. Schaefer, M. Schneider, C. Schall, C. Wagner, C.-M. Lehr, Optical tweezers reveal relationship between microstructure and nanoparticle penetration of pulmonary mucus, Proc. Natl. Acad. Sci. USA 109 (2012) 18355–18360, http://dx.doi.org/10.1073/pnas.1214066109.
[133] J.A. Cribb, P.A. Vasquez, P. Moore, S. Norris, S. Shah, M.G. Forest, R. Superfine, Nonlinear signatures in active microbead rheology of entangled polymer solutions, J. Rheol. 57 (2013) 1247–1264, http://dx.doi.org/10.1122/1.4811477.
[134] M. Radiom, R. Hénault, S. Mani, A.G. Iankovski, X. Norel, J.-F. Berret, Magnetic wire active microrheology of human respiratory mucus, Soft Matter 17 (2021) 7585–7595, http://dx.doi.org/10.1039/D1SM00512J.
[135] M. Papanikolas, M. Markovetz, D.B. Hill, N. Caughman, C. Edelmaier, M.G. Forest, R. Freeman, Chemical insights into the mucus flake burden in cystic fibrosis, 2023, UNC Preprint.
[136] P.A. Vasquez, Y. Jin, E. Palmer, D. Hill, M.G. Forest, Modeling and simulation of mucus flow in human bronchial epithelial cell cultures – Part I: Idealized axisymmetric swirling flow, PLoS Comput. Biol. 12 (2016) e1004872, http://dx.doi.org/10.1371/journal.pcbi.1004872.
[137] G.W. Scott Blair, The role of psychophysics in rheology, J. Colloid Sci. 2 (1947) 21–32, http://dx.doi.org/10.1016/0095-8522(47)90007-X.
[138] S.A. McKinley, L. Yao, M.G. Forest, Transient anomalous diffusion of tracer particles in soft matter, J. Rheol. 53 (2009) 1487–1506, http://dx.doi.org/10.1122/1.3238546.
[139] N. Caughman, M. Markovetz, M. Papanikolas, R. Freeman, D.B. Hill, M.G. Forest, Disentangling the signal from the noise in microrheology of human bronchial epithelial mucus with dense raft structures, 2023, Pre-Print UNC.
[140] E.M. Furst, T.M. Squires, Microrheology, Oxford University Press, 2017.
[141] J. Kirch, C.A. Ruge, C. Schneider, J. Hanes, C.-M. Lehr, Nanostructures for overcoming the pulmonary barriers: Physiological considerations and mechanistic issues, in: M.J. Alonso, N.S. Csaba (Eds.), Nanostructured Biomaterials for Overcoming Biological Barriers, The Royal Society of Chemistry, 2012, pp. 239–272, http://dx.doi.org/10.1039/9781849735292-00239.
[142] N.N. Sanders, S.C. De Smedt, J. Demeester, The physical properties of biogels and their permeability for macromolecular drugs and colloidal drug carriers, J. Pharm. Sci. 89 (2000) 835–849, http://dx.doi.org/10.1002/1520-6017(200007)89:7<835::AID-JPS1>3.0.CO;2-6.
[143] J. Fiegel, T. Brenza, R. Hamed, Controlled transport for pulmonary drug delivery, in: H.D.C. Smyth, A.J. Hickey (Eds.), Controlled Pulmonary Drug Delivery, Springer New York, New York, NY, 2011, pp. 143–163, http://dx.doi.org/10.1007/978-1-4419-9745-6_7.
[144] S.K. Lai, J.S. Suk, A. Pace, Y.-Y. Wang, M. Yang, O. Mert, J. Chen, J. Kim, J. Hanes, Drug carrier nanoparticles that penetrate human chronic rhinosinusitis mucus, Biomaterials 32 (2011) 6285–6290, http://dx.doi.org/10.1016/j.biomaterials.2011.05.008.
[145] A. Macierzanka, N.M. Rigby, A.P. Corfield, N. Wellner, F. Böttger, E.N.C. Mills, A.R. Mackie, Adsorption of bile salts to particles allows penetration of intestinal mucus, Soft Matter 7 (2011) 8077, http://dx.doi.org/10.1039/c1sm05888f.
[146] B.B. Mandelbrot, J.W. Van Ness, Fractional Brownian motions, fractional noises and applications, SIAM Rev. 10 (1968) 422–437, http://dx.doi.org/10.1137/1010093.
[147] D. Panja, Generalized Langevin equation formulation for anomalous polymer dynamics, J. Stat. Mech. 2010 (2010) L02001, http://dx.doi.org/10.1088/1742-5468/2010/02/L02001.
[148] J.L.A. Dubbeldam, V.G. Rostiashvili, A. Milchev, T.A. Vilgis, Fractional Brownian motion approach to polymer translocation: The governing equation of motion, Phys. Rev. E 83 (2011) 011802, http://dx.doi.org/10.1103/PhysRevE.83.011802.
[149] G. Guigas, M. Weiss, Sampling the cell with anomalous diffusion—The discovery of slowness, Biophys. J. 94 (2008) 90–94, http://dx.doi.org/10.1529/biophysj.107.117044.
[150] S.C. Weber, A.J. Spakowitz, J.A. Theriot, Bacterial chromosomal loci move subdiffusively through a viscoelastic cytoplasm, Phys. Rev. Lett. 104 (2010) 238102, http://dx.doi.org/10.1103/PhysRevLett.104.238102.
[151] D. Ernst, M. Hellmann, J. Köhler, M. Weiss, Fractional Brownian motion in crowded fluids, Soft Matter 8 (2012) 4886, http://dx.doi.org/10.1039/c2sm25220a.
[152] C.R. Esther, M.S. Muhlebach, C. Ehre, D.B. Hill, M.C. Wolfgang, M. Kesimer, K.A. Ramsey, M.R. Markovetz, I.C. Garbarine, M.G. Forest, I. Seim, B. Zorn, C.B. Morrison, M.F. Delion, W.R. Thelin, D. Villalon, J.R. Sabater, L. Turkovic, S. Ranganathan, S.M. Stick, R.C. Boucher, Mucus accumulation in the lungs precedes structural changes and infection in children with cystic fibrosis, Sci. Transl. Med. 11 (2019) eaav3488, http://dx.doi.org/10.1126/scitranslmed.aav3488.
[153] M.R. Markovetz, I.C. Garbarine, C.B. Morrison, W.J. Kissner, I. Seim, M.G. Forest, M.J. Papanikolas, R. Freeman, A. Ceppe, A. Ghio, N.E. Alexis, S.M. Stick, C. Ehre, R.C. Boucher, C.R. Esther, M.S. Muhlebach, D.B. Hill, Mucus and mucus flake composition and abundance reflect inflammatory and infection status in cystic fibrosis, J. Cyst. Fibros. 21 (2022) 959–966, http://dx.doi.org/10.1016/j.jcf.2022.04.008.
[154] Y. Ling, M. Lysy, I. Seim, J.M. Newby, D.B. Hill, J. Cribb, M.G. Forest, Measurement error correction in particle tracking microrheology, 2019, http://dx.doi.org/10.48550/arXiv.1911.06451.
[155] K. Zhang, K.P.R. Crizer, M.H. Schoenfisch, D.B. Hill, G. Didier, Fluid heterogeneity detection based on the asymptotic distribution of the time-averaged mean squared displacement in single particle tracking experiments, J. Phys. A 51 (2018) 445601, http://dx.doi.org/10.1088/1751-8121/aae0af.
[156] T. Savin, P.S. Doyle, Static and dynamic errors in particle tracking microrheology, Biophys. J. 88 (2005) 623–638, http://dx.doi.org/10.1529/biophysj.104.042457.
[157] P. Gniewek, A. Kolinski, Coarse-grained modeling of mucus barrier properties, Biophys. J. 102 (2012) 195–200, http://dx.doi.org/10.1016/j.bpj.2011.11.4010.
[158] A.G. Ford, X. Cao, M.J. Papanikolas, T. Kato, R.C. Boucher, M.R. Markovetz, D.B. Hill, R. Freeman, M.G. Forest, Molecular dynamics simulations to explore the structure and rheological properties of normal and hyper-concentrated airway mucus, Stud. Appl. Math. 147 (2021) 1369–1387, http://dx.doi.org/10.1111/sapm.12433.
[159] J. Israelachvili, R. Pashley, The hydrophobic interaction is long range, decaying exponentially with distance, Nature 300 (1982) 341–342, http://dx.doi.org/10.1038/300341a0.
[160] J.A. Anderson, J. Glaser, S.C. Glotzer, HOOMD-blue: A Python package for high-performance molecular dynamics and hard particle Monte Carlo simulations, Comput. Mater. Sci. 173 (2020) 109363, http://dx.doi.org/10.1016/j.commatsci.2019.109363.
[161] K. Kremer, G.S. Grest, Dynamics of entangled linear polymer melts: A molecular-dynamics simulation, J. Chem. Phys. 92 (1990) 5057–5086, http://dx.doi.org/10.1063/1.458541.
[162] H. Kamberaj, R.J. Low, M.P. Neal, Time reversible and symplectic integrators for molecular dynamics simulations of rigid molecules, J. Chem. Phys. 122 (2005) 224114, http://dx.doi.org/10.1063/1.1906216.
[163] J. Lawrimore, K. Bloom, Shaping centromeres to resist mitotic spindle forces, J. Cell Sci. 135 (2022) jcs259532, http://dx.doi.org/10.1242/jcs.259532.
[164] J.H. Gibcus, K. Samejima, A. Goloborodko, I. Samejima, N. Naumova, J. Nuebler, M.T. Kanemaki, L. Xie, J.R. Paulson, W.C. Earnshaw, L.A. Mirny, J. Dekker, A pathway for mitotic chromosome formation, Science 359 (2018) eaao6135, http://dx.doi.org/10.1126/science.aao6135.
[165] C.C. Correll, J. Bartek, M. Dundr, The nucleolus: A multiphase condensate balancing ribosome synthesis and translational capacity in health, aging and ribosomopathies, Cells 8 (2019) 869, http://dx.doi.org/10.3390/cells8080869.
[166] C.J. Lawrimore, K. Bloom, Common features of the pericentromere and nucleolus, Genes 10 (2019) 1029, http://dx.doi.org/10.3390/genes10121029.